CERES Edition-2 CLOUD PROPERTY RETRIEVALS USING TRMM VIRS AND TERRA AND AQUA MODIS DATA, PART I: ALGORITHMS

Patrick Minnis, Szedung Sun-Mack, David F. Young, Patrick W. Heck, Donald P. Garber, Yan Chen, Douglas A. Spangenberg, Robert F. Arduini, Qing Z. Trepte, William L. Smith, Jr., J. Kirk Ayers, Sharon C. Gibson, Walter F. Miller, Venkatesan Chakrapani, Yoshihide Takano, Kuo-Nan Liou, Yu Xie

Submitted to *IEEE Transactions on Geoscience and Remote Sensing*

December 2009

P. Minnis, D. F. Young, D. P. Garber, and W. L. Smith, Jr. are with the Science Directorate, NASA Langley Research Center, Hampton, VA 23681-0001 USA (email: Patrick.Minnis-1@nasa.gov)
S. Sun-Mack, Y. Chen, D. A. Spangenberg, R. F. Arduini, Q. Z. Trepte, J. K. Ayers, S. C. Gibson, W. F. Miller, and V. Chakrapani are with Science Systems and Applications, Inc., Hampton, VA 23666 USA.
P. W. Heck is with the NOAA Cooperative Institute for Meteorological Satellite Studies, Madison, WI 53706 USA.
Y. Takano and K.-N. Liou are with the Department of Oceanic and Atmospheric Sciences, University of California, Los Angeles, Los Angeles, CA 90095 USA.
Y. Xie is with the Department of Atmospheric Sciences, Texas A&M University, College Station, TX 77843 USA.

Abstract

The NASA Clouds and Earth's Radiant Energy System (CERES) Project is designed to improve our understanding of the relationship between clouds and the solar and longwave radiation fields. This is achieved using satellite broadband instruments to map the top-of-atmosphere radiation fields with coincident data from satellite narrowband imagers being used to retrieve the properties of clouds imbedded in those fields. This paper documents the end-to-end CERES Edition-2 cloud property retrieval system used to analyze data collected by the Tropical Rainfall Measuring Mission (TRMM) Visible Infrared Scanner (VIRS) and by the Moderate Resolution Imaging Spectroradiometer (MODIS) instruments onboard the Terra and Aqua satellites covering the period from 1998 through 2007. Two daytime cloud property retrieval methods are explained: the Visible Infrared Solar-infrared Split-Window Technique (VISST) used over snow-free surfaces, and the Shortwave-infrared Infrared Near-infrared Technique (SINT) used for snow or ice covered surfaces. The Shortwave-infrared Infrared Split-window Technique (SIST) used for all surface conditions at night is also described. These methods, in conjunction with appropriate ancillary data and empirical parameterizations of cloud thickness, are used to derive cloud boundaries and phase as well as optical depth, effective particle size, and condensed/frozen water path at both pixel and CERES footprint levels. Additional information is presented detailing the potential effects of satellite calibration differences, highlighting methods to compensate for spectral differences and correct for atmospheric absorption and emissivity, and discussing known errors in the code. Because a consistent set of algorithms, auxiliary input, and calibrations across platforms are used, instrument and algorithm-induced changes in the data record are minimized. This facilitates the use of the CERES data products for studying climate-scale trends.

I. INTRODUCTION

Understanding the relationship between clouds and solar and longwave radiation processes requires determination of the cloud distribution and radiation budget as well as the associated cloud microphysical and macrophysical properties. The NASA Clouds and Earth's Radiant Energy System (CERES) Project [1] was designed to facilitate this understanding by measuring the top-of-atmosphere radiation fields simultaneously with cloud properties using instruments onboard several satellites to provide global and diurnal coverage. The CERES scanners, which measure broadband shortwave and combined (total) shortwave and longwave radiances, operated on the Tropical Rainfall Measuring Mission (TRMM), *Terra* and *Aqua* satellites. Data from the TRMM Visible Infrared Scanner (VIRS) [2] and the *Terra* and *Aqua* Moderate Resolution Imaging Spectroradiometer (MODIS) [3] are used for discriminating between clear and cloudy scenes, and for retrieving the properties of clouds in the latter and the aerosols in the former. Those cloud properties, including cloud fraction, phase, temperature, height, optical depth, effective particle size, and condensed/frozen water path, are key parameters needed to link the atmospheric radiation and hydrological budgets. The CERES radiation measurements and their inversion as well as the methods for identifying cloudy pixels and retrieving aerosol properties in clear pixels have been described elsewhere [4-8]. This paper documents the CERES algorithms that have been used to derive cloud properties from the TRMM, *Terra*, and *Aqua* data taken between 1998 and 2007.

To study climate-scale trends, it was recognized that cloud and radiation fields must be determined using consistent algorithms, auxiliary input (e.g., atmospheric temperature and humidity profiles), and calibrations across platforms to minimize instrument- and algorithm-induced changes in the record. CERES planned to measure the complete diurnal cycle of clouds

and radiation for the Tropics and obtain unprecedented sampling of those same fields in the extra-tropics by combining data from the precessing-orbit TRMM with the late morning *Terra* and early afternoon *Aqua* observations. The requirements for consistency, simultaneity, and collocation between the cloud and radiation measurements necessitated the development of a set of algorithms and a processing system that was independent of other global cloud processing systems that were either operating or being developed prior to launch of the first CERES-bearing orbiter. Although cloud properties have been derived from geostationary and NOAA polar-orbiting satellites since 1983 by the International Satellite Cloud Climatology Project (ISSCP) [9], those products cannot be used because ISCCP samples the imager data at an effective resolution of ~32 km (larger than a CERES footprint, ~ 20 km), cloud particle size is assumed in the retrievals, and simultaneity with the CERES satellites is very limited. Like the ISCCP data, the Advanced Very High Resolution Radiometer (AVHRR) Pathfinder Atmospheres Extended (PATMOS-x) cloud products [10] were not usable because they have little simultaneity (< 5 min) with the satellites carrying the CERES scanners. Pixel-level cloud properties are derived from MODIS data by the MODIS Atmosphere Science Team (MAST), but they are retrieved with algorithms that use many of the 36 MODIS spectral bands [11,12] and auxiliary input data that are not necessarily consistent over time. The MAST algorithms, which have been used to generate the standard MAST products, i.e., MOD06/MYD06 and MOD35/MYD35 products from MODIS data [13], would be unable to yield cloud properties consistent with the standard MAST results when applied to the 5-channel VIRS data. Furthermore, CERES requires complete cloud information for each footprint and that is not always available in the standard MAST products.

The TRMM CERES scanner failed early in the mission obviating some of the consistency requirements, but other more important factors necessitated the development of independent cloud

and aerosol analysis algorithms. CERES is an end-to-end processing system with cloud properties feeding into subsystems that determine top of atmosphere (TOA), surface, and atmospheric radiative fluxes, including a complex, time-space averaging subsystem that employs geostationary satellite measurements [14]. The cloud detection and retrieval algorithms had to be responsive to the needs of the downstream processing systems and had to be as consistent as possible with the CERES geostationary satellite data processing system [14]. Given the limitations of external cloud datasets and the internal team interaction and consistency requirements, a unique set of cloud detection and retrieval algorithms was developed for CERES utilizing as few channels as possible while producing stable and accurate cloud properties that are compatible with the CERES anisotropic models.

This paper provides an overview of the algorithms used by CERES to retrieve cloud properties for pixels identified as cloudy by the CERES cloud mask [5]. Three distinct methods are used. During daytime, the Visible Infrared Shortwave-infrared Split-window Technique (VISST) is used over snow-free surfaces, while the Shortwave-infrared Infrared Near-infrared Technique (SINT) is applied when the background is identified as being covered by snow or ice. At night, the Shortwave-infrared Infrared Split-window Technique (SIST) is used over all surfaces. The theoretical bases for these algorithms have described elsewhere [15,16], so this paper serves to document the actual algorithms and their updates. A companion paper [17] presents examples of averaged results and comparisons with other datasets.

This is the second of four papers [5, 18, 19] that describe the CERES cloud analysis system for VIRS Edition 2 (Ed2), *Terra* Ed2, and *Aqua* Ed2. The initial, Edition 1 (Ed1), VIRS cloud property retrieval system (CPRS) was completed in 1998 and updated, along with *Terra* Ed1, to the VIRS and Terra Ed2 versions in 2003. The *Aqua* Ed2 CPRS is the same as that for *Aqua*

Edition 1a. Processing of VIRS and MODIS data for CERES using all 3 of the second edition algorithms described here began during 2004, beginning with data taken at each imager's start-of-operations date.

II. DATA

Figure 1 shows the flow of data into the CERES CPRS. The imager radiance data (Box I, Fig. 1) are processed in groups of pixels denoted as a tile. Each tile consists of an array of pixels defined by 16 scan lines with 8 or 16 elements for MODIS and VIRS, respectively. These arrays nominally correspond to 32 km x 32 km, a coverage obtained by sampling for MODIS. Although each pixel is analyzed individually, all pixels within a given tile use the same clear radiances and atmospheric corrections in the retrieval to increase computational efficiency. The input parameters used in the retrievals are explained below.

A. Satellite radiances

Because of the requirement for consistent retrievals among the various sensors, the CPRS nominally uses only 5 channels: 0.64 (visible, VIS), 1.6 (near-infrared, NIR), 3.8 (shortwave-infrared, SIR), 10.8 (infrared, IR), and 12.0 μm (split window, SW). For CERES, these channels are sequentially numbered 1 through 5. For *Aqua*, the 2.1-μm channel replaces the 1.6-μm channel (CERES reference channel 2) in this analysis due to shortcomings in the *Aqua* 1.6-μm channel. The calibrations of the relevant VIRS and MODIS channels are only briefly discussed here, because they have already been reviewed in detail [5].

1) VIRS: The VIRS scans in a cross-track mode out to a nadir angle of 45°, which translates to a maximum viewing zenith angle VZA (θ) of 48°. The TRMM orbit gives the VIRS a viewing perspective distinctly different from either geostationary or Sun-synchronous satellites and allows

it to sample all local times of day over a 46-day period. At the Equator, this sampling is evenly distributed over the period, but at higher latitudes (maximum of ~38°), the sampling is primarily in darkness for 2 weeks followed by 2 weeks of sunlight. The VIRS data were obtained from the NASA Langley Atmospheric Sciences Data Center.

Version-5a VIRS data are analyzed by CERES at full resolution. Changes to the VIRS channel calibrations, reviewed by Minnis et al. [5], include corrections of the NIR channel for a thermal leak at 5.2 μm and for a large (~18%) bias relative to its *Terra* MODIS counterpart. A slight day-night calibration discrepancy in the IR and SW channels is not taken into account here.

2) MODIS: Terra MODIS [3] began collecting data starting in late February 2000 from a Sun-synchronous orbit with a 1030-LT equatorial crossing time. *Aqua* MODIS became operational in July 2002 from a Sun-synchronous orbit with a 1330-LT equatorial crossing time. CERES ingests a 19-channel subset of the 36-channel MODIS complement with the intention of using additional channels in future editions of the algorithms and in subsystems outside the CPRS (for summary, see [5]). The 0.25-km channel-1 (VIS) pixels corresponding to the 1-km channel-1 pixels are also included in the ingested data for future use. To minimize processing time, the 1-km MODIS data are sampled by taking every other pixel and scan line. This subsetted dataset, provided by the NASA Goddard Space Flight Center Distributed Active Archive Center, was further reduced by sampling every other pixel during actual processing, yielding an effective resolution of ~2.8 km. For a given CERES footprint (~ 20 km at nadir for *Aqua* and *Terra,* ~10 km for VIRS), this additional subsampling yields cloud properties having small root mean square (rms) differences (e.g., 0.013 in cloud fraction) relative to those determined using the original subsetted sampling .

No calibration changes were applied to the MODIS data despite some discrepancies between *Aqua* and *Terra* at certain wavelengths. On average, the *Terra* SIR brightness temperatures are 0.55 K greater than those from *Aqua* during the daytime. At night, *Aqua* data having brightness temperatures $T_b > 250$ K vary linearly with *Terra*, in the manner observed during the daytime, with the *Terra* values typically exceeding their *Aqua* counterparts by 0.55 K. At lower temperatures, the *Terra* temperatures vary exponentially with their *Aqua* counterparts asymptoting to a value of 218 K as the *Aqua* values reach 197 K. The *Terra* VIS channel gain was found to drop by 1.17% after November 18, 2003, but otherwise had no trends. Prior to that date, the *Terra* VIS gain is 1% less than the *Aqua* gain. The *Aqua* reflectance is 4.6% greater, on average, than that from VIRS, a result that is consistent with the theoretical differences between the VIRS and MODIS spectral windows. During the day, the VIRS SIR brightness temperatures are 1.39 and 0.85 K less than the *Terra* and *Aqua* MODIS values, respectively. More details about these intercalibrations and those for other channels are provided in [5] and the references therein.

B. Ancillary data

1) Vertical profiles: Vertical profiles of temperature, humidity, wind, and ozone and total aerosol amounts comprise the CERES Meteorology, Ozone, and Aerosol (MOA) dataset (Box A, Fig. 1). The CERES MOA temperature, wind, and humidity profiles are based on numerical weather analyses (NWA): the European Centre for Medium-range Weather Forecasting (ECMWF) reanalyses for VIRS and the Global Modeling Assimilation Office Global Earth Observing System (GEOS) Model 4.03 analyses [20] for the MODIS processing through April 2006 and GEOS 5.0 thereafter. The ECMWF profiles were available at a nominal resolution of 0.5° every 6 hours and surface skin temperature T_{skin} was available every 3 hours. GEOS profiles

and skin temperatures were made available at the same temporal resolutions on a 1° grid. The ozone vertical profiles and total column concentration, are taken from the 2.5° National Centers for Environmental Prediction (NCEP) Stratosphere Monitoring Ozone Blended Analysis (SMOBA) [21] or from the Earth Probe Total Ozone Mapping Spectrometer (total column optical depth only) at a 1.25° resolution when SMOBA data are not available. All input MOA data are interpolated to a common 1° x 1° grid. These include surface skin temperature, height, and total column ozone, and profiles of temperature, specific humidity, and ozone at up to 58 pressure levels from the surface to 0.1 hPa [22].

2) Surface charcateristics: Surface type is used to select the surface albedos and emissivities, as well as to select which method is employed to retrieve cloud properties. Surface type (Box D, Fig. 1) is denoted with the variable *K* and given a value of 1-19 corresponding to one of the 19 modified International Geosphere Biosphere Programme (IGBP) surface types [23] listed in Table 1. The land percentage LP in each 10' IGBP grid box was computed from the 1-km IGBP land-water dataset. Daily ice and snow extent data (Box C, Fig. 1) are obtained from the Near Real-Time Equal Area Special Sensor Microwave Imager (SSM/I) Earth (EASE)-Grid Daily Global Ice Concentration and Snow Extent products [24] on a nominal 25-km polar stereographic grid and supplemented by the National Environmental Satellite Data and Information Service (NESDIS) Interactive Multisensor Snow and Ice Mapping System Daily Northern and Southern Hemisphere Snow and Ice Analysis in the vicinity of coastlines [25]. All snow and ice extent values are interpolated to a 10' grid. If the ice and snow map indicates that if the snow or ice percentage exceeds 0% or 50%, respectively, within a given tile and the scene is overcast, or more than 50% of the clear pixels within the tile are identified as snow, then the surface type is temporarily designated as $K = 15$, snow/ice.

Average land elevation was determined for each 10' region from the 1-km United States Geophysical Survey (USGS) GTOPO30 dataset (http://edc.usgs.gov/products/elevation/gtopo30/gtopo30.html). The percentage of water surface in a given 10' region was determined from the 1-km IGBP dataset. These data are included in Box D, Fig. 1.

3) Surface emissivity and albedo: Spectral surface emissivities ε_{si}, available on the 10' grid, are used in conjunction with the MOA skin temperatures to estimate the clear-sky radiances for the CERES reference channels, i = 3,5, where the wavelengths are listed in Table 2. These emissivities have been discussed in detail elsewhere [5].

When channels 1-3 are used in the retrievals during daytime, the surface bidirectional reflectance ρ_s and diffuse albedo α_{sd} are used to determine the reflected radiation field underneath the cloud. For channel 1, α_{sd} and ρ_s are estimated, respectively, from the diffuse clear-sky albedo α_{csd1} at a solar zenith angle (SZA) of 53° and from the clear-sky reflectance, ρ_{cs1}, as described by (3) and (4) in [5]. The channel 2 and 3 albedos and reflectances are estimated in a more direct manner. The surface or clear-sky reflectances and diffuse albedos for each channel are obtained either from the prescribed values (Boxes E and H, Fig. 1) used in the cloud mask or from clear pixels within the tile (Box K, Fig. 1) resulting from the cloud mask. The latter are used if more than 10% of the tile is clear.

The prescribed values for the VIS and NIR channels over water surfaces are taken from an updated version of the VIS bidirectional reflectance distribution function (BRDF) of [26]. For land and snow surfaces, the VIS overhead-sun clear-sky albedos $\alpha_{cs1}(\mu_o=1)$ and overhead-sun NIR surface albedos $\alpha_{s2}(\mu_o=1)$ based on bi-daily updated 10' global maps are passed through

from the CERES cloud mask. These quantities and the sources for their values are discussed further by [5]. The quantity $\mu_o = \cos(\theta_o)$, where θ_o is the SZA.

The VIS diffuse clear-sky albedo is estimated at a given SZA for any 10' region as

$$\alpha_{csd1} = \delta_{cs1}(K, \mu_o=0.6)\ \alpha_{cs1}(\mu_o=1), \tag{2}$$

where δ_{cs1} is the normalized directional reflectance model that predicts the variation of the clear-sky albedo with SZA for a given surface type.

The VIS clear-sky reflectance is estimated as

$$\rho_{cs1}(\mu_o,\mu,\phi) = \delta_{cs1}(K,\mu_o)\ \alpha_{cs1}(\mu_o=1)\ \chi_1(K, \mu_o,\mu,\phi), \tag{3}$$

where χ_1 is the VIS BRDF, $\mu = \cos\theta$, and ϕ is the relative azimuth angle.

For the NIR channels, the diffuse surface albedo for any 10' region is estimated as

$$\alpha_{sd2} = \delta_{sN}(K,\mu_o=0.6)\ \alpha_{s2}(\mu_o=1), \tag{4}$$

where the subscript, *2*, indicates either 1.6 or 2.1-μm. The surface reflectance is,

$$\rho_{s2}(\mu_o,\mu,\phi) = \delta_{s2}(K,\mu_o)\ \alpha_{s2}(\mu_o=1)\ \chi_{s2}(K,\mu_o,\mu,\phi), \quad (5)$$

where χ_{s2} is the NIR BRDF. The VIS and NIR BRDFs are the same as those used in [5].

The SIR reflectances and albedos are based on the surface emissivity. During daytime, solar radiation in the SIR channel is reflected by the surface in addition to the thermal emission from the surface. To account for this reflected contribution, the SIR or channel-3 surface reflectance is estimated as

$$\rho_{s3} = (1-\varepsilon_{s3})\,\chi_{sN}(K;\mu_o,\mu,\phi), \quad (6)$$

The BRDFs used for the 2.1-μm channel were also used for channel 3 because of the lack of bidirectional reflectance measurements at SIR wavelengths. An exception is the theoretical 3.8-μm snow reflectance model [27], which is used here for all snow and ice surfaces. Since the SZA dependence of the SIR albedo is unknown, the diffuse SIR albedo is estimated simply as

$$\alpha_{sd3} = (1-\varepsilon_{s3}). \quad (7)$$

C. Cloud reflectance and emittance models

The cloud water droplet and solid hexagonal column ice crystal distributions described by Minnis et al. [28] were used to compute reflectance lookup tables (LUTs) for channels 1-3 and coefficients used in the emittance parameterizations for channels 3-5. For the VIS channel, the

same optical properties listed by [28] were used in the adding doubling (AD) radiative transfer model to develop higher angular resolution LUTs: 21 regularly spaced (0.05 intervals) μ_o and μ nodes between 0 and 1, and 24 ϕ nodes with higher resolution near the extrema. The AD model used 350 Legendre polynomials and 120 Fourier terms to deconvolve the water droplet and ice crystal scattering phase functions. The VIS LUTs cover the VIS optical depth τ range from 0.25 to 128 for droplet effective radii r_e between 2 and 32 μm and ice crystal effective diameters D_e between 6 and 135 μ m. Because effective diameter is defined as in [29], it is not directly comparable to the effective radius. However, for comparisons to other retrievals, the equivalent effective radius can be computed using the following formula. For ice,

$$r_e = (7.918 \times 10^{-9}\ \mu m^{-2}\ D_e^2 + 1.0013 \times 10^{-3}\ \mu m^{-1}\ D_e + 0.4441)\ D_e. \quad (8)$$

The VIS reflectance LUTs described in [30] are used to estimate the reflectance due to Rayleigh scattering in the atmosphere. It should be noted that Table 5 in [28] reproduced the wrong data giving the average volume and area for each of the effective ice crystal sizes. The correct values are given here in Table 3. The values of D_e and ice water path in the retrievals are not based on those values and, therefore, the misprinted values in Table 5 of Minnis et al. [28] have no impact on the results.

The VIS angular resolutions and deconvolutions were also used for the NIR and SIR calculations. The NIR optical properties for ice and water were computed using Mie scattering calculations as in [28] and ray-tracing results as in [31] covering the same optical depth range as the VIS models. In addition, cloud absorptances $A_{2c}(r,\tau,\mu_o)$ were computed as functions of

particle size, optical depth, and μ_o. These were integrated over μ_o to obtain the diffuse solar absorptance $A_{2cd}(r,\tau)$. All of the calculations are referenced to the VIS optical depth.

Similarly, new values for the SIR optical properties were computed as in [28] and [31] using the MODIS and VIRS spectral filter functions. In this instance, however, the reflectances were computed separately for 0.1-μm sub-bands between 3.5 and 4.0 μm using the single-scattering albedos and extinction coefficients determined from Mie scattering calculations for liquid water droplets with the indices of refraction from [32] for each sub-band. The scattering phase functions are based on Mie scattering computations for the spectral-response-weighted indices of refraction. The sub-band reflectances were then integrated over the spectral response function weighted by the TOA incoming radiances [33] to obtain a single reflectance for the band.

Figure 2, which plots the refractive indices of liquid water over the spectral response functions for AVHRR, VIRS, and MODIS, shows that the real index of refraction (Fig. 2a) for each of those bands varies linearly across the instruments' spectral bands. On the other hand, the value of the imaginary index of refraction (Fig. 2b) is a minimum near the bands' central wavelengths (~3.78 μm) so that the absorption is greater at all wavelengths away from the center. Thus, when the response is used to compute reflectance or absorption and convolved over the incoming solar radiances or for terrestrial radiances, the reflectance or absorption, respectively, will be less or greater than that if the indices of refraction were integrated over the spectral filters to obtain an effective index of refraction for the band. This is illustrated in Fig. 3 for the VIRS 3.8-μm channel. The maximum reflectances for a 6-μm water droplet model (Fig. 3a) are 0.29 and 0.27 using the effective indices of refraction and the solar weighted reflectances, respectively. Similarly for a 12-μm droplet model (Fig. 3b), the maximum reflectance is 0.142 for the effective wavelength versus 0.130 for the solar weighted model. Thus, the retrieved value

of r_e will be smaller using the solar-weighted reflectances compared to that retrieved using the effective wavelength calculated reflectances.

The sub-band weighting for ice is accomplished in a similar manner using the indices of refraction from [34] to compute the optical properties for ice spheres having the same effective radii as the ice crystal size distributions. The sub-band values were integrated to obtain a band average that is used to compute a normalization factor relative to the band average for the original ice crystal calculations. The ice-sphere sub-band values were then adjusted with the normalization factor to obtain the sub-band ice crystal optical properties and the reflectances were computed for each sub-band using the AD model. The spectral integration and solar-weighting were performed in the same manner as for the liquid droplet models. The SIR reflectance LUTs are limited to $\tau \leq 32$ since the reflectances asymptote to their maximum values at smaller optical depths for all of the considered particle sizes.

The channel-3 effective emittances were determined in a similar manner using the same sub-bands. In this instance (Fig. 2b), the blackbody curve of the cloud temperature (not shown) substitutes for the solar-spectrum to weight the absorption and emission computed for each sub-band in the final integration over the response function. The results were used to compute the model effective emittances for each particle size, optical depth, and pairs of surface and cloud temperatures, and to develop the emittance parameterizations as in [28].

III. METHODOLOGIES

As shown in Fig. 4, the CPRS selects one of three methods to retrieve cloud properties based on the SZA and the surface type. A tile is considered to be in daylight if SZA < 82°. Although pixels having SZA between 82° and 90° are technically in daylight, they are processed with the

nighttime retrieval algorithm including all modeled solar reflectances where appropriate. For a given tile, the atmospheric attenuation is first computed for every layer and channel for use in any of the techniques, except where noted otherwise. The appropriate parameterizations are then employed to estimate the TOA spectral radiances for each pixel based on the surface albedo or skin temperature and emissivity and the atmospheric attenuation parameters. Each method iteratively finds the best match between the model-predicted and observed radiances to determine the cloud phase, cloud effective radiating temperature T_c, cloud effective height Z_c, τ, and the effective particle size r, which can be either r_e or D_e, depending on cloud phase. The ice water path *IWP* and liquid water path *LWP* are computed as functions of the products of τ and the appropriate effective particle size. Using adjusted MOA temperature profiles and empirical fits for cloud base, the algorithm computes the effective cloud pressure p_c, cloud-top height Z_t and pressure p_t, and cloud-base height Z_b and pressure p_b.

A. Atmospheric absorption and emission corrections

The atmospheric absorption and emission corrections are primarily based on calculations using the correlated *k*-distribution method (CKD) [35] with coefficients developed for the VIRS and MODIS channels used here (see [36] and http://asd-www.larc.nasa.gov/~kratz/). The NIR atmospheric corrections are discussed in section III.B.4.

1) VIS absorption: For the VIS channel, only ozone and water vapor absorption are considered although there are a few other absorbing species with negligible impact. All ozone absorption is computed using the same approximation as in [30] and, although assumed to occur in the stratosphere above any clouds, the ozone concentration u is computed in cm STP for the layer between the TOA and 300 hPa. Thus, the ozone transmittance is

$$t_{O3} = \exp\text{-}\{u\ (0.085 - 0.00052\ u)\ (1/\mu_o + 1/\mu)\}. \quad (9)$$

Further analysis after Ed2 processing began revealed that (9) overestimates the ozone optical thickness for the MODIS VIS channel by 13%, causing average overestimates of τ that increase exponentially from 1% or less for $\mu_o > 0.50$ up to 50% or more for $\mu_o < 0.12$. Thus, these biases become significant only for large SZAs and mainly affect the optical depths over high-latitude snow-free areas.

A parameterization of water vapor transmission t_{W1j} was developed for channel 1, based on radiative transfer calculations using the CKD method, to compute the cumulative layer water vapor transmissions starting from the top of the atmosphere and working downward toward the surface:

$$t_{W1j} = 0.9999 - 0.0046\ u_{wj} + 0.00007\ u_{wj}^2, \quad (10)$$

where the atmospheric path length is

$$u_{wj} = \mathrm{PW}_j\ (1/\mu_o + 1/\mu), \quad (11)$$

and PW_j is the precipitable water in atmosphere-cm. The subscript j denotes the layer from the TOA to pressure level j in the atmospheric profile. The total VIS atmospheric transmittance for layer j in the troposphere is the product of t_{O3} and t_{W1j}. Water vapor absorption below the cloud is

ignored. Atmospheric molecular scattering is taken into account in the VIS reflectance parameterization. All aerosol scattering is assumed to occur below the cloud and is implicitly included in the surface reflectance and albedo.

2) Thermal channels: The atmospheric transmittances for channels $i = 3 – 5$ are calculated in a common manner, except that the SIR solar beam transmittance is computed separately from the atmospheric radiances and the VIRS SIR band is broken into 5 sub-bands, while only a single band is used for MODIS because it is much narrower [36]. The CKD method again is used to compute the layer optical depths τ_{ij}, and the transmittances and emitted radiances for each cumulative layer are computed starting at the TOA and working downward. The downwelling emitted radiances L_{Dij} and transmissivities t_{Dij} are computed as cumulative diffuse radiances from the TOA to the base of layer j, using the radiance at $\mu = 0.6$, while the upwelling transmissivities t_{Uij} and radiances L_{Uij} are computed only in the VZA direction, starting at the surface and working upward to the TOA, where they are designated with the subscript o. The surface is denoted with the subscript J. The downwelling SIR solar component is computed in the SZA direction, μ_o, using as the source term, the solar constant at 3.8–μm adjusted for the Earth-Sun distance and SZA. The nominal values of the SIR solar constants E_o are 10.51 and 10.77 W m^{-2} μm^{-1} sr^{-1}, for VIRS and MODIS, respectively. The CKD calculations include contributions from weak water vapor lines for all 3 channels, chlorofluorocarbons for VIRS 10.8 and 12.0 μm, the water vapor continuum for 10.8 and 12.0 μm, CO_2 for MODIS 10.8 and 12.0 μm, and CH_4 for 3.8 μm and N_2O for VIRS 3.8 μm. The Planck function evaluated at the central wavelength for each channel (Table 3) is used to convert temperature to radiance and vice versa. The layer optical depths are computed for the entire band.

B. Parameterizations of TOA reflectance and brightness temperatures

1) Visible reflectance parameterization: In the initial formulation of VISST used in VIRS Ed 1, the VIS reflectance was estimated using the parameterization developed by [30]. Further examination of that method found some relatively large errors over bright surfaces at certain angles. To improve the accuracy of the modeled VIS TOA reflectance for clouds over dark and bright surfaces, a new parameterization was developed using the results from a detailed adding-doubling (AD) radiative transfer model [30]. This parameterization is based on the AD equations using the LUTs developed in [28] for the diffuse cloud albedo $\alpha_{cd}(\tau, r)$, cloud albedo $\alpha_c(\tau, r, \mu_o)$, and the cloud reflectance $\rho_c(\tau, r, \mu_o, \mu, \phi)$, where τ and r are the cloud visible optical depth and effective particle size, respectively. The parameterization also uses the LUTs of atmospheric reflectance $\rho_R(\tau_R, \mu_o, \mu, \phi)$, albedo $\alpha_R(\tau_R,\mu_o)$, and diffuse albedo $\alpha_{Rd}(\tau_{DR},\mu_o)$ due to Rayleigh scattering [30]. It assumes that the atmosphere is divided into three layers with a lower surface. The top layer, designated layer 1, and layer 3 are Rayleigh scattering layers, while layer 2 is the cloud layer.

The reflectance for two adjacent layers is computed using the adding equations. These are then added to the third layer to yield the combined model surface and atmosphere TOA VIS reflectance R_{as}. Since the adding process is only approximated in this parameterization, there are residual differences between the AD model results and the initial parameterizations. These differences ΔR were parameterized further in terms of the scattering angle and used to adjust R_{as} to estimate the TOA reflectance,

$$R_{TOA} = (R_{as} + \Delta R) \exp(-\tau_{gas}(1/\mu + 1/\mu_o). \quad (12)$$

The exponential term accounts for gaseous absorption above the cloud and, in practice, varies with the altitude of the cloud. This formulation does not explicitly account for any aerosols; the surface albedo and reflectance are actually more representative of the surface and aerosols combined. The Appendix describes the parameterizations in detail.

When used for retrievals, the values of ΔR are computed for the specified values of α_{sd}, p_c, and r by linear interpolation and extrapolation between the values used to create the coefficients for (12). This equation was tested for a wider range of various cloud models, surface albedos, and cloud pressures than were used in the formulation of the parameterization. The resulting relative differences between (12) and the AD calculations for those cases plus the original cases used in the formulation are summarized in the Appendix.

2) Infrared brightness temperature parameterization: The simple model of brightness temperature used here is that the observed radiance for channels 3 - 5 can be represented as

$$B_i(T_i) = L_{Uio} - L_{Uij\text{-}1} + t_{\mathrm{Uio}}\{[1-\varepsilon_i(\tau_i,r;\mu)][(1 - \varepsilon_{si})(L_{DiJ} - L_{Dij}) + \varepsilon_{si} B_i(T_{skin})] + \varepsilon_i(\tau_i,r;\mu) B_i(T_c) / t_{\mathrm{Uij\text{-}1}}\}, \quad (13)$$

where T_i is the equivalent blackbody temperature, T_c is the cloud effective radiating temperature, B is the Planck function, ε_{si} is the surface emissivity, and the effective cloud emittance ε_i approaches unity as the cloud becomes optically thick. The first two terms represent the radiance contributed by the atmosphere above the cloud while the second term includes the radiances from the cloud and the surface attenuated by the atmosphere. The downwelling radiation from the cloud is neglected. If scattering in the cloud is neglected,

$$\varepsilon_{ai} = 1 - \exp(-\tau_{ai} / \mu), \tag{14}$$

where the absorption optical depth $\tau_{ai} = (1 - \varpi_o)\tau_i$ and ϖ_o is the single-scattering albedo. As noted earlier, T_s is taken either from the MOA dataset or from the clear portion of the tile.

3) Shortwave infrared brightness temperature parameterization during daytime: The use of the SIR data during the daytime complicates (13) because of solar reflectance at those wavelengths. The observed radiance has an additional term:

$$B_3(T_3) = L_3' + \mu_o d_o E_o t_{U3o} t_{D3J} \rho_{c3}, \tag{15}$$

where L_3' is computed with (13), d_o is the Earth-sun distance correction, and the combined surface and cloud reflected component is

$$\rho_{c3} = [\rho_3(\tau, r;\mu_o, \mu,\phi) / t_{U3j\text{-}1}] + [t_{D3o} / t_{D3J}] [1 - \varepsilon_{a3} - \alpha_{c3}(\tau,r;\mu_o)] \rho', \tag{16}$$

where

$$\rho' = [1 - \varepsilon_{a3} - \alpha_{c3}(\tau,r;\mu)] \rho_{s3}(\mu_o,\mu,\phi) + [1 - \alpha_{cd3}(\tau,r) - \varepsilon_{ad}]\alpha_{cd3}(\tau)\alpha_{sd3}^2, \tag{17}$$

α_{c3}, α_{cd3}, and ρ_3, from the channel-3 reflectance LUTs, represent the cloud albedo for a given incident angle, the diffuse cloud albedo, and the cloud bidirectional reflectance. The first term in (16) accounts for the reflectance directly from the cloud, while the second term accounts for the contribution of the surface to the reflectance. It is approximated as a combination of primary and

secondary surface reflectances. The primary assumes reflectance of the direct beam in the direction of the sensor and the secondary assumes that the second reflectance is diffuse and reflects the radiation originally reflected by the surface and scattered back by the cloud. Since the secondary term is usually very small relative to the first term, it and higher order reflectances were neglected in the VIRS, *Terra*, and *Aqua* Ed2 cloud analyses.

4) Near-infrared reflectance parameterization: Since the atmospheric scattering at NIR wavelengths is negligible and all aerosol reflectance is assumed to occur underneath the cloud, the formulation for the model is simpler than that for either the VIS or SIR channels. The theoretical TOA NIR reflectance, which was formulated to match AD radiative transfer computation results over a wide range of conditions, is approximated as

$$\rho_2 = \rho_{2c}\,(m,\tau,\mu_o,\mu,\phi)\,\exp(-\tau_{2a1}\,[1/\mu_o + 1/\mu])$$

$$+ \alpha_{s2}\,\exp(-(\tau_{2a1}\,[1/\mu_o + 2.04] + 4.08\,\tau_{2a2}))\;(1 - \alpha_{2cd} - A_{2cd})\;(1 - \alpha_{2c} - A_{2c}). \qquad (18)$$

The first term is the direct bidirectional reflectance of the model cloud attenuated by the atmosphere above the cloud, corresponding to the atmospheric absorption optical depth for layer 1, τ_{2a1}. The second term represents the contribution of the surface to the TOA reflectance and only includes two-way diffuse absorption by layer 2 under the cloud, τ_{2a2}. For snow-covered regions, the second term is typically negligible because the NIR surface albedos are often less than 0.1 [19]. The atmospheric absorption at NIR wavelengths is due to weak water vapor, CO_2, CH_4, and, at 2.1-μm only, N_2O bands. The total atmospheric column optical depth at 1.6 μm varies from ~0.021 in a subarctic winter atmosphere to ~0.024 in a tropical atmosphere. Thus, a simple

parameterization was developed to estimate the atmospheric absorption as a function of latitude for different levels in the atmosphere. The 2.1-μm atmospheric absorption optical depth is greater and can range from ~0.05 in a subarctic winter atmosphere up to ~0.16 in a tropical atmosphere. The absorption optical depths are computed explicitly at 2.1 μm for each tile using the CKD method. Unfortunately, in the *Aqua* Ed2 algorithm, the 1.6-μm atmospheric absorption optical depths were mistakenly used for the 2.1-μm retrievals. This error causes an underestimation of the retrieved optical depths. The extent of the bias is explored in [17].

C. Retrieval techniques for cloud temperature, phase, optical depth and particle size

1) VISST: The iterative process employed by the VISST is shown schematically in Fig. 5. It is much like the approach pioneered by Han et al. [37] for deriving liquid water cloud microphysical properties from AVHRR data and was initially formulated and applied to AVHRR data for both ice and liquid water clouds by Minnis et al. [38] and Young et al. [39]. The IR, VIS, and SIR radiances are primarily sensitive to changes in T_c, τ, and r_e, respectively, a basis used for a variety of similar techniques [13, 37, 40, 41]. Nominally, for a given pixel, the iterative process is performed for each phase, beginning with an initial guess of r_e' = 8 μm and $T_c = T(Z = 3$ km) for liquid clouds and D_e = 45 μm and $T_c = T(Z_c = 9$ km). However, if $T_4 < 233$ K, it is assumed that the pixel contains an ice cloud and only the ice loop (A) is executed.

Values of R_{TOA} are computed for each case using (12) and interpolated to match the observed VIS reflectance to yield τ and ε_4, which is then used to recompute T_c with (13). These parameters are then used to compute T_3' using (15) for each particle size model, yielding minimum and maximum values, T_{3min}', and T_{3max}', respectively. If it is the first iteration and the observed value, T_3, is either smaller than T_{3min}' or greater than T_{3max}', the assumed particle size is reset to the

maximum or minimum particle size, respectively, and τ and T_c are recomputed and the process is repeated in the second iteration. If T_3 is outside of either model extreme after the first iteration, then it is assumed that no retrieval is possible with that set of models. If T_3 is within the extreme model values during any iteration, then r_e is estimated by interpolating between the values of T_3' to match T_3. For water clouds, if $|r_e - r_e'| < 0.5$ μm, the iteration stops, otherwise a new value of r_e' is computed as the average of r_e and the original r_e', and the process is repeated. A no-retrieval value results if convergence does not occur after 20 iterations. The same procedure is used for the ice clouds, except that the ice crystal models replace their water droplet counterparts and the iteration stops when $|D_e - D_e'| < 2.5$ μm.

The cloud thermodynamic phase is selected using a set of sequential tests. These are illustrated in Figs. 6-7 for the Aqua Ed2 algorithm. If the observed reflectance is less than the clear-sky value, it is likely a no-retrieval pixel and is assigned the mean layer results (depending on T_4), if it is not reclassified as clear (Fig. 6). This assignment is given on the assumption that it is a shaded cloud. If there is only one phase solution and T_c is physically reasonable, the phase is accepted for that solution. If T_c is unreasonable, than it follows the same path as the no solution case. If there are dual phase solutions, a simple temperature check is applied: if $T_c > 273$ K ($\leq$ 233 K) for both results, the liquid (ice) solution is used, unless the ice cloud is over snow. Otherwise, a more complicated series of tests are applied. These further tests incorporate results from two other separate algorithms, the Layer Bispectral Threshold Method (LBTM) [42] and a supervised classifier (denoted as UAH) based upon a back-propagation neural network [43]. The latter provides an independent assessment of cloud and surface type and is primarily used over snow surfaces. The former uses a two-dimensional VIS-IR histogram to provide an estimate of the cloud layer that includes the pixel. It also determines a parameter, designated "hi_cold", that

indicates whether or not there is at least one pixel in the high layer having T_4 less than the warmest pixel in the low cloud layer. This parameter is used to reclassify thin cirrus pixels that would otherwise be called liquid cloud pixels. It was introduced to minimize such classifications, which occurred in the Terra Ed2 results at certain viewing and illumination angles. The remaining tests shown in Figs. 6 and 7 make use of the LBTM and UAH output, the particle sizes, T_c, τ, and the surface types to arrive at final solution. The Terra Ed2 algorithm follows a similar flow but it does not employ the LBTM results. It uses the ratio of the 1.6 and 0.65-μm reflectances to aid the phase selection.

Figure 8 shows an example of the VISST pixel-level results for Terra MODIS data taken over western North America and the adjacent Pacific Ocean at ~21 UTC, 12 June 2004. The pseudocolor red (VIS), green (NIR), blue (IR) or RGB image (Fig. 8a) shows a complex scene with low clouds over much of the water, high clouds over the northern part of the image and a mixture of high and low clouds over land. Sunglint is apparent off the coast of southern California between cloud decks. The phase image (Fig. 8b) shows the liquid water clouds in blue, ice clouds in white, clear areas in green, and no retrievals in pink. Effective temperatures (Fig. 8c) for the ice clouds range from 215 K to 260 K, while T_c for the liquid clouds varies from 294 K to less than 265 K. The retrieved values of D_e (Fig. 8d) are between 15 and 100 μm, compared to a range of 6 to 27 μm for r_e (Fig. 8e). The largest values of r_e are over the water, while the smallest values of D_e tend to occur where the ice clouds appear to overlap lower clouds. This type of variation is expected if the high cloud is optically thin because the reflected SIR radiance from the low cloud will yield an underestimate of D_e [44]. The retrieved optical depths (Fig. 8g) vary from slightly less than 0.5 up to the maximum of 128. The resulting LWP ranges up to ~ 500 gm^{-2}, while the IWP is as large as 1500 gm^{-2} for some pixels near the top of the image (Fig. 8h). For overlapped

clouds, the IWP is an estimate of the total cloud water path TWP, which includes both ice and water. Typically, it overestimates TWP [44]. The cloud effective height Z_c (Fig. 8f) and effective pressure p_c (Fig. 8i) are estimated from T_c as described in section III.E.

2) SIST: The primary goal of the nighttime retrievals is to adjust cloud temperature and, hence, the height for semi-transparent clouds to provide some consistency between day and night. Although the SIST derives particle size and optical depth for clouds it identifies as optically thin, those parameters are considered to be experimental and are only included in the output for future study. The theoretical basis and heritage of the SIST and relevant references are provided by [15]. The SIST relies on the brightness temperature differences (BTD) between channels 3 and 4 (BTD_{34}) and between channels 4 and 5 (BTD_{45}) to solve for T_c, τ, and r_e or D_e.

Given an optically thin cloud ($\tau < 6$), μ, and the background (theoretically, it can be either clear or cloudy below) temperatures for channels 3, 4, and 5, it is assumed that a given pair of BTD_{34} and BTD_{45} at a particular value of T_4 uniquely defines a cloud characterized by T_c, r_e or D_e, and τ. These parameters are determined by matching the three measured quantities as closely as possible to the same parameters calculated using (13). Each observed quantity should fall between the corresponding pair of discrete theoretical calculations for a given phase. The distance in *BTD* from the model value to the observed value for both channels 3 and 5 is used to interpolate between each model and parameter to assign a value of T_c, r_e or D_e, and τ to the pixel. In the absence of temperature constraints ($T_c > 273$ K or $T_c < 233$ K), the phase is selected based on how closely the channel 3 and 5 parameters agree with each other.

This technique attempts to determine τ, T_c, and particle size through an iterative process that minimizes the differences between model-derived and observed values of BTD_{34} and BTD_{45} for the observed T_4. This procedure, illustrated schematically in Fig. 9, begins with input values of μ

and T_s and assumes an initial value of $T_c = T'(k)$, where $T'(k) < T_4$ and k is an index corresponding to the emittance model for a particular particle size and phase. The first guess temperature is equal to $0.5(T_4 + 183)$. For each of the channel-4 emittance models, $\tau[T'(k), k]$ is determined using a secant iteration method to match T_4. The iteration is confined to temperatures between $T_4 + 3$ K and $T_p - 2$ K, where T_p is the tropopause temperature. The arrow in Fig. 9a represents this process. The resulting value of τ is used to compute T_3 and T_5 using the channel-3 and 5 emittance models in (13). The model values of $BTD_{34}[T'(k), k]$ and $BTD_{45}[T'(k), k]$, shown as the intersections of the model curves and dashed line in Fig. 9a, are calculated from the model-derived temperatures and T_4. Difference errors, $e_{34} = BTD_{34} - BTD_{34}[T'(k), k]$ and $e_{45} = BTD_{45} - BTD_{45}[T'(k), k]$, are computed for each model. The composite error,

$$e[T'(k), k] = e_{34}^2 + e_{45}^2, \tag{19}$$

is minimized in the iteration process. These operations are repeated varying $T'(k)$ as illustrated in Fig. 9b until $e(T_{new}, r_e)$ is minimized yielding the best estimate of cloud temperature for model k. In the first iteration, $T'(k)$ is increased by 10 K for each step until e begins to increase. Figure 10a depicts how e can vary with increasing $T'(k)$. Subsequent iterations repeat the error calculations using increasingly smaller temperature increments bounded by the last two temperatures used in the preceding iteration. The iterations continue until the increment is less than 0.1 K or up to 15 times. In the latter case, the results from the penultimate iteration are accepted. If the resultant optical depth exceeds 16, then τ is reset to 16. For the case in Fig. 10a, the value of $T_c(k)$ corresponds to the minimum error. This entire procedure is repeated again for each model producing final values of $e[T'(k), k]$ as shown in Fig. 10b. In practice, the algorithm begins with the smallest model for the phase and continues until e_{34} and e_{45} switch signs, which indicates that

the observation is between the previous two models. One of the two models, k_{min1}, will have the smallest value of e for the particular phase, while the other model, k_{min2}, should also have a relatively low error. These two models are then selected for interpolation. If $T_c > 273$ K or < 233 K, only the water-droplet or ice-crystal models, respectively, are used.

Final values of r_e or D_e, T_c, and τ are computed for channel 3 by linearly interpolating between $r_e(k_{\min 1})$ and $r_e(k_{min2})$, $T_c(k_{min1})$ and $T_c(k_{min2})$, and $\tau(k_{min1})$ and $\tau(k_{min2})$, respectively, using $e_{34}[T'(k_{min1}), k_{min1}]$ and $e_{34}[T'(k_{min2}), k_{min2}]$ as the independent variables. The same interpolation is repeated for channel 5. The resultant values for the two channels are averaged to obtain the best estimate of each parameter. If both phases are considered, then the results for the phase having the smallest uncertainty,

$$e_{35} = \left(\frac{T_{c3} - T_{c5}}{T_{c3}} \right)^2 + \left(\frac{\tau_3 - \tau_5}{\tau_3} \right)^2 + \left(\frac{r_{e3} - r_{e5}}{r_{e3}} \right)^2, \qquad (20)$$

are selected for the final parameter values. The subscripts 3 and 5 refer to the parameter values derived using channel 4 with channels 3 and 5, respectively. The most accurate estimates of T_c are obtained for the larger optical depths ($\tau > 6$), while the most accurate values of τ and r_e should occur for $1 < \tau < 6$. There is little variation in BTD with particle size for small and large optical depths. This method was tested using a limited set of simulated data with superimposed noise. In these cases, the retrieved particle sizes were within 0.1 μm of the simulated cloud values and the phase was chosen correctly.

The iteration procedures comprise only one part of the complete SIST, which is illustrated schematically in Figure 11. Given the input parameters, it is first determined if the cloud is colder than its background. If $T_4 > T_s$, a set of default values are applied. Otherwise, the input parameters checked to see of the cloud is likely to be optically thick based on BTD_{34} and, if so, a phase is

selected based on the temperature. The threshold for determining whether it is optically thin or thick is

$$\Delta T_{34} = 0.095\,(T_4 - T_s) - 4.175. \qquad (21)$$

This formula was derived from a set of radiative transfer computations using a wide range of particle sizes and a range of optical depths up to 16. A relatively conservative threshold, it does not eliminate all clouds having $\tau > 16$ and is imposed mainly to facilitate processing. The clouds determined to be thick at this point are given a default value of $\tau = 32$. If $BTD_{34} \geq \Delta T_{34}$, then the iterative procedures are applied either using one phase or both. If solutions for both phases are determined, then the final model selection depends on e_{35} as noted earlier.

Figure 12 shows an example of the retrieved properties from the SIST for an Aqua image taken over the North Atlantic (the Azores are located in lower center of the image) at ~23 UTC, 22 May 2004. The RGB image (Fig. 12a), based on T_4, T_5, and BTD_{34}, reveals a swath of high clouds associated with a frontal system at the bottom and low clouds with broken overlapping high clouds north of the frontal system. Most of the apparent high clouds are identified as ice clouds in the phase image (Fig. 12b). For the ice clouds, T_c varies from 205 to 257 K (Fig. 12c), while it is between 253 and 280 K for most of the water clouds. The resulting values of D_e (Fig. 12d) range from less than 18 to 135 μm, the maximum possible value. The maximum and minimum model values occur in a variety of conditions, particularly when τ is very low or high or in multi-layered clouds. Default values of $D_e = 24$ or 64 μm are evident over many areas, while non-extreme retrieved values are mostly associated with $0.5 < \tau < 2$ (Fig. 12g). The extreme

values tend to occur outside this range of τ because D_e is sensitive to small errors in the atmospheric corrections and background temperatures at smaller and larger values of τ as seen in [15]. Most of the water droplet clouds yield r_e between 7 and 14 μm (Fig. 12e). The larger values are mostly default values of r_e = 12 μm, corresponding to τ = 32 (red in Fig. 12g).

3) SINT: The Shortwave-infrared Infrared Near-infrared Technique (SINT) is based on the method pioneered by Platnick et al. [16]. It is applied when the VIS clear-sky reflectance is extremely high, i.e., when the surface is covered with snow and/or ice. Determination of the background surface as snow or ice comes either from the scene classification for adjacent clear pixels or from snow and ice maps. Because snow and ice are not very reflective at NIR wavelengths, the NIR channel replaces the VIS channel in the iteration used by the VISST, effectively serving as the channel responsive to changes in cloud optical depth. The SIR channel is still used to retrieve the effective particle size. Thus, the iteration follows that in Fig. 5 with all VIS reflectances replaced by their NIR counterparts using the parameterizations and atmospheric corrections described earlier. The phase selection is the same as for the VISST except no information is available from the LBTM or the NIR/VIS ratio.

Figure 13 presents an example of the SINT retrievals using Terra MODIS data taken over the Arctic Ocean and part of northern Canada at 23 UTC, 3 May 2005. The RGB image (Fig. 13a.) shows areas with various shades of magenta and red that usually correspond to snow or ice-covered surfaces. The peachy or yellowish colors are usually due to low clouds, while the whiter areas are generally colder liquid or ice clouds. Most of the cloudy pixels (Fig. 13b) were interpreted as being composed of liquid droplets (blue) while the optically thinner clouds (Fig. 13g) were retrieved as ice clouds (white). The values of T_c range from 243 to 269 K (Fig. 13c) indicating that all of the clouds could be comprised of supercooled liquid droplets. The effective

ice diameter values (Fig. 13d) vary from less than 18 μm to more than 109 μm, while r_e is generally between 6 and 16 μm. The overlap in particle size between the ice and liquid clouds suggests that some of the ice clouds could actually be liquid or vice versa, or mixed phase. These potentially ambiguous phase results are typical for optically thin clouds over snow. The values of Z_c (Fig. 13f) and p_c (Fig. 13i) indicate that the liquid clouds are quite low, being mostly above 900 hPa and below 1 km in the top half of the image. The ice clouds may be as high as 6 km corresponding to p_c < 500 hPa. Cloud optical depth ranges from 0.5 to 32, while the corresponding cloud water paths (Fig.13h) reach up ~500 gm^{-2}.

In Fig. 13h and other panels, some areas appear as clear rectangles in obviously cloudy areas. These are regions where the ice/snow map was read improperly and the surface was classified as free of snow and ice, but the background albedo was that of permanent snow and ice. Thus, the VISST was used and all the observed VIS radiances were less than the clear-sky predicted values, so no retrieval could be performed and the tile was classified as clear. This snow-ice map mismatch was mainly a problem for Terra Ed2a and was reduced significantly for Aqua Ed2.

D. Cloud water paths

The values of IWP and LWP are computed based on the assumption that the retrieved effective particle sizes represent the average over the entire cloud thickness. For liquid water,

$$LWP = 4\, r_e\, \tau / 3Q, \tag{22}$$

where the extinction efficiency Q ranges from 2.03 to 2.19 for r_e ranging from 32 to 4 μm [28]. The IWP was computed for each D_e model using the ratios of the cross-sectional areas to

volumes in Table 2 and the values of Q found in Table 8 of [28]. A cubic equation was fit to the results yielding a smooth function in terms of D_e with an rms error of 1%:

$$IWP = \tau\,(0.259\,D_e + 0.819 \times 10^{-3}\,D_e^2 - 0.880 \times 10^{-6}\,D_e^3). \quad (23)$$

E. Cloud heights and pressure

Several different cloud heights and pressures are derived to estimate the vertical extent of the detected clouds. These parameters are cloud effective height and pressure, cloud-top height and pressure, cloud thickness, and cloud base height and pressure.

1) Cloud effective height: The cloud effective height Z_c and pressure p_c are defined as the lowest altitude and corresponding pressure, respectively, where T_c is found in the profile. Vertical profiles of temperature and pressure measured by radiosondes and output from NWAs often fail to miss the extreme temperature changes near the tops of the boundary-layer inversions [45-48]. The results typically overestimate cloud-top height for low clouds because the cloud-top temperature observed by the satellite is often found higher in the temperature profile than at the actual location of the boundary-layer inversion. To overcome this sounding bias when relating cloud temperature to altitude, the lower portion of the temperature profile in the CPRS is first adjusted based on the surface temperature and a fixed lapse rate.

The temperature profile is adjusted using an adaptation of the techniques developed by [46, 49]. For $p > 700$ hPa, a simple lapse rate anchored to a surface temperature T_o is used to define the temperature profile. That is,

$$T(z + z_o) = T_o + \Gamma\,(z - z_o), \quad (24)$$

where z_o is the surface elevation above mean sea level and Γ is the lapse rate. Over ocean and land surfaces, the value of T_o is, respectively, the sea surface temperature and the running 24-h mean surface air temperature from NWA reanalyses. Following Minnis et al. [46], Γ = -7.1 K km^{-1}. Between 700 and 500 hPa, Γ is adjusted to ensure that the resulting temperature at 500 hPa equals that in the NWA profile. For $p \leq$ 500 hPa, the NWA vertical profile of atmospheric temperature remains unchanged. If $T_o < T_c$, then Z_c is set, as a default, to 0.5 km above the surface elevation. The pressure corresponding to Z_c is assigned to p_c.

2) Cloud-top height: Because the value of T_c corresponds more closely to the center of the cloud in optically thin cases [50] and to some depth below the cloud top for optically thick clouds, e.g. [48], it differs from the actual physical top of the cloud. For cirrus clouds, a strong correlation was found between emissivities defined relative to the physical cloud-top temperature T_t and the cloud effective temperature [50]. Here, that type of relationship is used to estimate T_t and, thereby, the physical cloud-top height Z_t and pressure p_t from the temperature profile. In many cases, the value of T_t is found for channel 4 by substituting the cloud-top emissivity ε_t for ε_4, T_t for T_c, and T_4 for T_i in (12), then solving for T_t.

For ice clouds having $T_c < 245$ K and $\tau \leq 2$, the regression fit from Minnis et al. [51] is used to find ε_t:

$$\varepsilon_t = \varepsilon_4 \, (2.966 - 0.009141 \, T_c). \tag{25}$$

If $\varepsilon_t > \varepsilon_4$, ε_t is set equal to ε_4. If $2 < \tau \leq 6$, ε_t is found by linearly interpolating in τ between the result of (25) and ε_4 using τ values of 2 and 6 as the respective independent variables. For all clouds having $\tau > 6$, $\varepsilon_t = \varepsilon_4$. Similarly, for ice clouds having $T_c > 245$ K and $\tau \leq 2$,

$$\varepsilon_t = \varepsilon_4 \, (0.00753 \, T_c - 1.12). \qquad (26)$$

This equation is based on linear interpolation between the results of (25) and the water cloud values at 280 K. For other clouds having $T_c > 245$ K and $\tau > 2$, ε_t is found in the same manner as for clouds having $T_c \leq 245$ K, except (26) is used in place of (25) for the interpolations.

For liquid water clouds having $\tau > 6$, $\varepsilon_t = \varepsilon_4$. If $\tau < 2$, $\varepsilon_t = 0.99 \, \varepsilon_4$. For clouds having $2 < \tau \leq 6$, ε_t is found by linearly interpolating in τ between the result of (25) and ε_4 using τ values of 2 and 6 as the respective independent variables. This difference between ε_t and ε_4 is very small for water clouds because the differences between the cloud top and effective heights for water clouds are usually less than 0.2 km, which is less than the accuracy of the height determination.

After the initial value of T_t is computed for clouds having $T_c < 265$ K, additional adjustments are made if $2 < \tau \leq 6$. A new value of T_t is found by linearly interpolating in τ between the original value of T_t and T_t' using τ values of 2 and 6 as the respective independent variables, where

$$T_t' = 0.622 \, T_c + 77.7 \text{ K}, \qquad (27a)$$

for $T_c < 242$ K and

$$T_t' = 1.012 \, T_c - 14.0 \text{ K}, \qquad (27b)$$

for 265 K $< T_c \leq 242$ K. If $T_t' > T_c - 2$ for $T_c < 242$ K, T_t' is reset to T_c - 2. The adjustments represented by (27) and the interpolations were developed from additional unpublished

comparisons of surface radar and satellite-based cloud top temperatures. And finally, T_t is constrained to be less than or equal to the tropopause temperature.

One final adjustment is made after Z_t is determined from T_t to ensure that there is a reasonable depth to the layer above Z_c in high clouds. If $Z_t > 6$ km and $Z_t - Z_c < 0.333$ km, 0.5 K is subtracted from T_t and Z_t is recomputed, T_t remains greater than the tropopause temperature.

3) Cloud-base height and thickness: Cloud base height is estimated as $Z_b = Z_t - \Delta Z$. The cloud base pressure p_b is determined from Z_b and the NWA vertical pressure profile. The cloud thickness ΔZ is computed in km using empirical formulae. For all liquid water clouds,

$$\Delta Z = 0.39 \ln \tau - 0.01, \tag{28}$$

if $\tau > 1$. Otherwise,

$$\Delta Z = 0.085 \tau^{1/2}. \tag{29}$$

The minimum allowable ΔZ is 0.02 km. Equation (28) is taken from [52], while (29) is based on the results of [46]. For ice clouds with $T_c \leq 245$ K,

$$\Delta Z = 7.2 - 0.024 T_c + 0.95 \ln \tau. \tag{30}$$

This parameterization is a blend of the results from [52] and [53]. The minimum thickness for these clouds is also 0.02 km, with a maximum of 8 km. For ice clouds with $T_c > 245$ K, the cloud thickness is estimated by linearly interpolating in temperature between ΔZ for a liquid cloud at

275 K and for an ice cloud at 245 K.

F. Pixel-level and CERES Single Scanner Footprint (SSF) Products

The pixel-level data are convolved with the individual broadband CERES radiative fluxes to obtain the Single Scanner Footprint (SSF) dataset as described briefly by [1]. Figure 14 illustrates the structure of an SSF. When obtaining mean properties for each CERES footprint, each imager pixel is assigned a weight corresponding to the point spread function of the footprint. The weights are greatest near the pixel center and decrease outwards from the center in an asymmetrical fashion. The weights are used in computing cloud fraction and all other associated parameter values within the footprint. In addition to a wide range of radiative parameters and ancillary information, the SSF includes the cloud fraction and means of the associated properties for up to two cloud layers. The overlapping clouds illustrated in Fig. 14 are interpreted as a single cloud layer and assigned to either the low or high layer depending on the thickness of the upper layer. Values for Z_t, Z_b, and ΔZ are not included, but can be estimated from p_t and p_b, which are part of the SSF complement. The content of the SSF and other CERES products is described in detail by [54].

To account for the no-retrieval pixels within a footprint, the SSF convolution assigns the mean cloud properties from cloudy pixels in the footprint with retrieved values to the no-retrieval pixels, if more than 1/9 of pixels in the footprint have valid cloud retrievals. Otherwise, only the valid cloudy pixels are used and the no-retrieval pixels are not considered as part of the total number of pixels in the footprint. Cloud properties could not be retrieved for 6.6% of pixels classified as cloudy during the daytime, 7.5 and 5.6% for Terra and Aqua, respectively. At night, only 1.4% of the cloudy pixels are inconsistent with the parameterizations. Most no-retrieval

pixels occur in polar regions over snow-covered surfaces or over very bright deserts. In the former instance, the SINT is unable to find a match, probably because of uncertainties in the clear-sky reflectance fields. In the latter case, the pixels detected as clouds may actually be heavy concentrations of aerosols that are misclassified as clouds. Over most ocean and land areas outside of the polar regions and the Sahara Desert, the no-retrievals account for only 1 - 2% of the total number of cloudy pixels.

Imager pixel-level results are retained for imager granules containing data that correspond to a selected number of locations around the globe. These granules are used for visual assessment and for comparison to independent validation datasets obtained from several research facilities around the world, e.g., [48]. The pixel-level results are also used to compute various statistics for quality control purposes. The statistics include monthly, seasonal, and longer term averages of the various properties. (The quality control products are available at http://lposun.larc.nasa.gov/~cwg/.)

VI. Concluding Remarks

This paper documents the CERES Ed2 cloud property retrieval algorithms, which have been applied to both Terra and Aqua MODIS data through December 2007 and to TRMM VIRS data through July 2001. The Ed2 processing will continue through, at least, 2010 and beyond until CERES Edition 3 processing begins. These algorithms, based on radiatively consistent cloud effective temperatures and optical depths, utilize a variety of empirical methods to crudely characterize the cloud vertical structure. A more refined approach is being developed for CERES Edition 3 that will have new parameterizations and explicit retrievals of some overlapping cloud systems. Since the techniques described herein primarily rely on the few channels that are

common to most modern meteorological satellite imagers, they can be applied to analyze the radiance data and obtain cloud properties for many of those satellites [55, 56].

Examples of the instantaneous results were shown to illustrate the techniques. The companion paper [17] provides examples of the cloud property averages derived from the quality control products. Known systemic problems (e.g., ozone transmittance) have been identified here and will be corrected in CERES Edition 3. Further discussion of the uncertainties and validation of the Ed2 results is also provided by [17] along with comparisons of the results to those from other sources. Alone, the available Ed2 data should be quite valuable for studying cloud variability. The combined CERES clouds and flux products (e.g., SSF) are unique and are already helping to improve our understanding of the relationships between clouds and the radiation budget.

APPENDIX

A VIS reflectance parameterization was developed to improve the accuracy of the estimated TOA reflectances for clouds over both dark and bright surfaces. This parameterization is based on the adding-doubling (AD) method and replaces terms in the AD equations using values in the LUTs developed in [28] for the diffuse cloud albedo $\alpha_{cd}(\tau, r)$, cloud albedo $\alpha_c(\tau, r, \mu_o)$, and the cloud reflectance $\rho(\tau, r, \mu_o, \mu, \phi)$, where τ and r are the cloud visible optical depth and effective particle size, respectively. The relative azimuth angle is represented by ϕ. The parameterization also uses the LUTs of atmospheric reflectance $\rho_R(\tau_R, \mu_o, \mu, \phi)$, albedo $\alpha_R(\tau_R,\mu_o)$, and diffuse albedo $\alpha_{Rd}(\tau_{dR},\mu_o)$ due to Rayleigh scattering [30]. The parameterization assumes the atmosphere is divided into three layers above a surface. The top layer, designated layer 1, and layer 3 are Rayleigh scattering layers, while layer 2 is the cloud layer.

The reflectance for two adjacent layers is computed using the adding equations. The combined reflectance for the top Rayleigh layer and the cloud layer is

$$R_{12} = \rho_{R1} + \alpha_c{}' D_1(1 - \alpha_{Rd1}) + t_{R1}(\mu)\,[t_{R1}(\mu_o)\,\rho_c + S_1] \tag{A1}$$

where

$$\alpha_c{}' = \alpha_c\, t_{R1}(\mu_o) + [1 - t_{R1}(\mu_o)]\,\alpha_{cd}, \tag{A2a}$$

$$D_1 = T_1\,(1 + S_1), \tag{A2b}$$

$$S_1 = \alpha_{Rd1}\,\alpha_{cd} / (1 - \alpha_{Rd1}\,\alpha_{cd}), \tag{A2c}$$

$$T_1 = 1 - t_{R1}(\mu_o) - \alpha_{R1}, \tag{A2d}$$

$$\mu,\ \mu_o = \cos\theta,\ \cos\theta_o, \tag{A2e}$$

t_R is the direct Rayleigh transmission as defined in [30], and the numeric indices refer to a layer or combination of layers. The downward transmittance of the two layers is

$$T_{12} = D_1\,[T_2 + t_c(\mu)] + T_2\,t_{R1}(\mu_o), \tag{A3}$$

where

$$T_2 = 1 - \alpha_c{}' - t_c(\mu_o) \tag{A4}$$

and t_c is the direct transmittance of the cloud [30].

The combined reflectance for the three layers is

$$R_{123} = R_{12} + \alpha_{Rd2}\,D_2\,T_{12}{}^* + (\rho_{R2}\,t_c(\mu_o)\,t_{R1}(\mu_o) + S_2)\,t_c(\mu)\,t_{R1}(\mu), \tag{A5}$$

where

$$D_2 = T_{12}\,(1 + S_2), \tag{A6a}$$

$$S_2 = Q_2 / (1 - Q_2), \tag{A6b}$$

$$Q_2 = \alpha_{Rd2}\, R_{12}', \tag{A6c}$$

$$R_{12}' = \alpha_{R1} + (1 - \alpha_{Rd1}) D_1\, \alpha_{cd} + t_{R1}(\mu)[\alpha_{cd}\, t_{R1}(\mu_o) + S_1) \tag{A6d}$$

$$T_{12}^* = U_1^*\,(1 - \alpha_{Rd1}), \tag{A6e}$$

and

$$U_1^* = (1 - \alpha_{cd})\,(1 + S_1). \tag{A6f}$$

The downward transmittance for the three layers is

$$T_{123} = D_2\,[T_3 + t_c(\mu)] + T_2\, t_{R1}(\mu_o), \tag{A7}$$

where

$$T_3 = 1 - \alpha_{Rd2} - t_{R2}(\mu_o). \tag{A8}$$

The combined atmosphere and surface reflectance is

$$R_{as} = R_{123} + \alpha_{sd} T_{123}^*\, D_3 + t_{123}(\mu)[\rho_s\, t_{123}(\mu_o) + S_3], \tag{A9}$$

where α_{sd} and ρ_s are the diffuse surface albedo and surface bidirectional reflectance, respectively,

$$t_{123}(\mu) = t_{R1}(\mu)\, t_c(\mu)\, t_{R3}(\mu), \tag{A10a}$$

$$t_{123}(\mu_o) = t_{R1}(\mu_o)\, t_c(\mu_o)\, t_{R3}(\mu_o), \tag{A10b}$$

$$D_3 = T_{123}\,(1 + S_3), \tag{A10c}$$

$$S_3 = Q_3 / (1 - Q_3), \tag{A10d}$$

$$Q_3 = \alpha_{sd}\, R_{123}', \tag{A10e}$$

$$T_{123}^* = T_{12}^*\, U_2^*, \tag{A10f}$$

$$U_2^* = (1 + S_2^*)\,(1 - \alpha_{Rd2}), \tag{A10g}$$

$$S_2^* = R_{12}^*\, \alpha_{Rd2} / (1 - R_{12}^*\, \alpha_{Rd2}), \tag{A10h}$$

$$R_{12}^* = \alpha_{cd} + U_1^*\, \alpha_{Rd1}\,(1 - \alpha_{cd}), \tag{A10i}$$

and

$$R_{123}' = R_{12}' + \alpha_{Rd2} D_2 T_{12}^* + [S_2 + \alpha_{R2} t_c(\mu_o) t_{R1}(\mu_o)] t_{R1}(\mu) t_c(\mu). \tag{A10j}$$

Values for α_{sd} and ρ_s are estimated from the input clear-sky diffuse albedo α_{csd} [29] and the observed clear-sky reflectance, ρ_{cs}.

$$\alpha_{sd} = 1.149\, \alpha_{csd} - 0.0333. \tag{A11}$$

$$\rho_s = \rho_s' - D\, \alpha_{sd} / \exp(-\tau_{R13}/\mu_o), \tag{A12}$$

where

$$\rho_s' = [\rho_{cs} / \exp(-\tau_{gas} (1/\mu + 1/\mu_o)) - \rho_{R13}] / (1 - \alpha_{Rd13}), \quad \text{(A13a)}$$

$$D = (1 + S)(1- \alpha_{R13} - \exp(-\tau_{R13}/\mu_o) + S \exp(-\tau_{R13}/\mu_o), \quad \text{(A13b)}$$

$$S = \alpha_{sd} \alpha_{Rd13} / (1 - \alpha_{sd} \alpha_{Rd13}), \quad \text{(A13c)}$$

and τ_{gas} is the absorption optical depth for the gaseous absorbers, such as ozone and water vapor, for the particular visible channel being used. This formulation does not explicitly account for any aerosols, so that the surface albedo and reflectance are actually more representative of the surface and aerosols combined.

Equation (A9) was evaluated by comparing the values of R_{as} based on the LUTs with detailed AD computations for the same set of surface, cloud, and viewing and illumination conditions. These conditions are comprised of a total of 12 surface albedos ranging from 4 to 90%, 12 cloud optical depths between 0.5 and 128, 8 values of θ from 0.0° to 72.5°, 10 values of θ_o from 0.0°to 81.4°, and 15 values of ϕ. Two water droplet clouds with effective droplet radius r_e = 6 and 16 μm were used at cloud pressures p_c = 500 and 900 hPa. Two ice cloud models with effective ice crystal diameter D_e = 24 and 123 μm were used at p_c = 200 and 600 hPa. To minimize the error in the parameterization, the residual differences ΔR (r, τ, p_c, α_{sd}) between the results from the AD calculations and (A9) were fitted to the following polynomial:

$$\Delta R = a_o + \sum_{i=1}^{3} a_i \mu_o^{\,i} + \sum_{i=1}^{3} b_i \mu^i + \sum_{i=1}^{6} c_i \Theta^i , \quad \text{(A14)}$$

where Θ is the scattering angle in radians. The TOA reflectance for this parameterization, then, is

$$R_{TOA} = (R_{as} + \Delta R) \exp(-\tau_{gas}(1/\mu + 1/\mu_o). \quad \text{(A15)}$$

The exponential term accounts for gaseous absorption above the cloud and, in practice, varies with the altitude of the cloud.

When used for retrievals, the values of ΔR are computed for the specified values of α_{sd}, p_c, and r by linear interpolation and extrapolation between the values used to create the coefficients for (A14). Equation (A15) was tested for a wider range of various cloud models, surface albedos, and cloud pressures. The resulting relative differences between (A15) and the AD calculations for those cases plus the original cases used in the formulation are summarized in Table A1 under the heading, "new parameterization." Results from the old parameterization [30] are also shown to demonstrate the increase in accuracy and precision over the full range of surface albedos. The largest instantaneous errors occur for extreme values of θ, while the largest average errors for a given parameter occur for $\tau < 0.1$. For example, the greatest average difference for a given ϕ in the low albedo range is 0.9% for $\tau = 0.5$ at $\phi = 180°$. Thus, if the AD TOA reflectance ρ_{TOA} is 6% at $\phi = 180°$, the average value from (A15) is 6.1%. Overall, the differences are comparable to those between a high-resolution AD model and a discrete ordinates radiative transfer model (Y. Hu, personal communication 2001).

ACKNOWLEDGMENT

This research was sponsored by the NASA Earth Science Division of the Science Mission Directorate through the CERES Project. Thanks to Tim Marvel of Science Systems and Applications, Inc. for his assistance with the graphics.

REFERENCES

[1] B. A. Wielicki et al., "Clouds and the Earth's Radiant Energy System (CERES): Algorithm overview," *IEEE Trans. Geosci. Remote Sens.*, vol. 36, pp. 1127-1141, 1998.

[2] C. Kummerow, W. Barnes, T. Kozu, J. Shine, and J. Simpson, "The Tropical Rainfall Measuring Mission System (TRMM) sensor package," *J. Atmos. Oceanic Technol.*, vol. 15, pp. 809-827, 1998.

[3] W. L. Barnes, T. S. Pagano, and V. V. Salomonson, "Prelaunch characteristics of the Moderate Resoluiton Imaging Spectroradiometer (MODIS) on EOS-AM1," *IEEE Trans. Geosci. Remote Sens*., vol. 36, pp. 1088-1100, 1998.

[4] N. G. Loeb, K. J. Priestley, D. P. Kratz, E. B. Geier, R. N. Green, B. A. Wielicki, P. O'R. Hinton, and S. K. Nolan, "Determination of unfiltered radiances from the Clouds and the Earth's Radiant Energy System instrument," *J. Appl. Meteorol.*, vol. 40, pp. 822-835, 2001.

[5] P. Minnis, Q. Z. Trepte, S. Sun-Mack, Y. Chen, D. R. Doelling, D. F. Young, D. A. Spangenberg, W. F. Miller, B. A. Wielicki, R. R. Brown, S. C. Gibson, and E. B. Geier, "Cloud detection in non-polar regions for CERES using TRMM VIRS and Terra and Aqua MODIS data," *IEEE Trans. Geosci. Remote Sens.*, vol. 46, 3857-3884, 2008.

[6] Q. Trepte, P. Minnis, and R. F. Arduini, "Daytime and nighttime polar cloud and snow identification using MODIS data," *Proc. SPIE 3rd Intl. Asia-Pacific Environ. Remote Sensing Symp.,* Hangzhou, China, October 23-27, vol. 4891, 449-459, 2002.

[7] A. Ignatov and L. L. Stowe, "Physical basis, premises, and self-consistency checks of aerosol retrievals from TRMM VIRS," *J. Appl. Meteorol.*, vol. 39, pp. 2259-2277, 2000.

[8] A. Ignatov, A., P. Minnis, N. Loeb, B. Wielicki, W. Miller, S. Sun-Mack, D. Tanre, L. Remer, I. Laszlo, and E. Geier, "Two MODIS aerosol products over ocean on the Terra and Aqua CERES SSF datasets," *J. Atmos Sci.*, 62, pp.1008-1031, 2005.

[9] W. B. Rossow and R. A. Schiffer, "Advances in understanding clouds from ISCCP," *Bull Am. Meteor. Soc.*, vol. 80, pp. 2261-2287, 1999.

[10] S. M. Thomas, A. K. Heidinger, and M. J. Pavolonis, "Comparison of NOAA's operational AVHRR-derived cloud amount to other satellite-derived cloud climatologies," *J. Climate*, vol. 17, pp. 4805-4822, 2006.

[11] S. A. Ackerman, K. I. Strabala, W. P. Menzel, R. A. Frey, C. C. Moeller, and L. E. Gumley, "Discriminating clear sky from clouds with MODIS," *J. Geophys. Res.*, vol. 103, pp. 32 141–32 157, 1998.

[12] M. D. King et al., "Cloud and aerosol properties , precipitable, water, and profiles of temperature and water vapor," *IEEE Trans. Geosci. Remote Sens.*, vol. 41, pp. 442-458, 2003.

[13] S. Platnick, M. D. King, S. A. Ackerman, W. P. Menzel, B. A. Baum, J. C. Riedl, and R. A. Frey, "The MODIS cloud products: Algorithms and examples from Terra," *IEEE Trans. Geosci. Remote Sens.*, vol. 41, pp. 459-473, 2003.

[14] Young, D. F., P. Minnis, G. G. Gibson, D. R. Doelling, and T. Wong, "Temporal interpolation methods for the clouds and Earth's Radiant Energy System (CERES) Experiment," J. Appl. Meteorol., vol. 37, pp. 572-590, 1998.

[15] Minnis, P., et al., 1995: "Clouds and the Earth's Radiant Energy System (CERES) Algorithm Theoretical Basis Document, Volume III: Cloud Analyses and Radiance Inversions (Subsystem 4)", NASA RP 1376 vol. 3, pp. 135-176, 1995.

[16] Platnick, S., J. Y. Li, M. D. King, H. Gerber, and P. V. Hobbs, "A solar reflectance method for retrieving cloud optical thickness and droplet size over snow and ice surfaces," J. Geophys. Res., vol. 106, 15185-15199, 2001.

[17] P. Minnis, S. Sun-Mack, Y. Chen, M. M. Khaiyer, P. W. Heck, William L. Smith, Jr., Ricky R. Brown, D. A. Spangenberg, L. Nguyen, Y. Yi, B. Lin, R. Palikonda, M. L. Nordeen, J. K. Ayers, X. Dong, B. Xi, and E. B. Geier, "CERES Edition 2 cloud property retrievals using TRMM VIRS and Terra and Aqua MODIS data: Part II: Examples of averaged results and comparisons with other data," *IEEE Trans. Geosci. Remote Sens.*, submitted, 2009.

[18] Trepte, Q. Z, P. Minnis, D. A. Spangenberg, R. F. Arduini, S. Sun-Mack, and Y. Chen, "Polar cloud and snow discrimination for CERES using MODIS data," IEEE Trans. Geosci. Remote Sens., in preparation fof submission, 2010.

[19] Sun-Mack, P. Minnis, Y. Chen, R. F. Arduini, and D. F. Young, "Visible clear-sky and near-infrared surface albedos derived from VIRS and MODIS data for CERES," IEEE Trans. Geosci. Remote Sens., in preparation for submission, 2010.

[20] Bloom, S., A. da Silva, D. Dee, M. Bosilovich, J.-D. Chern, S. Pawson, S. Schubert, M. Sienkiewicz, I. Stajner, W.-W. Tan, M.-L. Wu, "Documentation and Validation of the Goddard Earth Observing System (GEOS) Data Assimilation System - Version 4 ," Technical Report Series on Global Modeling and Data Assimilation 104606, 165 pp., 26, 2005.

[21] Yang, S.-K., S. Zhou, and A. J. Miller, "SMOBA: A 3-dimensional daily ozone analysis using SBUV/2 and TOVS measurements.", 2006 (http://www.cpc.ncep.noaa.gov/products/stratosphere/SMOBA/smoba_doc.shtml)

[22] Gupta, S. K., N. A. Ritchey, F. G. Rose, T. L. Alberta, T. P. Charlock, and L. H. Coleman, "Regrid humidity and temperature fields (system 12.0). CERES Algorithm Theoretical Basis Document Release 2.2," NASA RP 1376, 20 pp., 1997. (http://asd-www.larc.nasa.gov/ATBD/ATBD.html)

[23] Belward, A. S., J. E. Estes, and K. D. Kline, "The IGBP-DIS 1-Km Land-Cover Data Set DISCover: A Project Overview," Photogrammetric Engr. and Remote Sens., vol. 65, p. 1013-1020, 1999.

[24] Nolin, A., R.L. Armstrong, and J. Maslanik, "Near Real-Time SSM/I EASE-Grid Daily Global Ice Concentration and Snow Extent, January to March 2004," National Snow and Ice Data Center, updated daily, 1998. (http://nsidc.org/data/docs/daac/nise1_nise.gd.html)

[25] Ramsay, B. H., "The interactive multisensor snow and ice mapping system," Hydrol. Processs., vol. 12, pp. 1537-1546, 1998.

[26] Minnis, P. and E. F. Harrison, "Diurnal variability of regional cloud and clear-sky radiative parameters derived from GOES data, Part I: Analysis method," J. Clim. Appl. Meteorol., vol. 23, pp. 993-1011, 1984.

[27] Trepte, Q., P. Minnis, and R. F. Arduini, "Daytime and nighttime polar cloud and snow identification using MODIS data," Proc. SPIE 3rd Intl. Asia-Pacific Environ. Remote Sensing Symp. 2002, Hangzhou, China, October 23-27, vol. 4891, 449-459, 2002.

[28] Minnis, P., D. P. Garber, D. F. Young, R. F. Arduini, and Y. Takano, "Parameterization of reflectance and effective emittance for satellite remote sensing of cloud properties," J. Atmos. Sci., vol. 55, 3313-3339, 1998.

[29] Ou, S. C., K. N. Liou, W. M. Gooch, and Y. Takano, "Remote sensing of cirrus cloud parameters using Advanced Very High Resolution Radiometer 3.7- and 10.8-µm channels," Appl. Opt., vol. 32, 2171-2180, 1993.

[30] Minnis, P., Y. Takano, and K.-N. Liou, "Inference of cirrus cloud properties using satellite-observed visible and infrared radiances, Part I: Parameterization of radiance fields," J. Atmos. Sci., vol. 50, 1279-1304, 1993.

[31] Takano, Y. and K.-N. Liou, "Radiative transfer in cirrus clouds: I. Single scattering and optical properties if oriented hexagonal ice crystals," J. Atmos. Sci., vol. 46, 3-19, 1989.

[32] Hale, G. M. and M. R. Querry, "optical constants of water in the 200-nm to 200-µm wavelength region," Appl. Opt., vol. 12, pp. 555-563, 1973.

[33] Wehrli, C., "Extraterrestrial Solar Spectrum," pub. 615, Physikalisch-Meteorologisches Observatorium Davos and World Radiation Center, Davos-Dorf, Switzerland, 1985.

[34] Warren, S. G., "Optical constants of ice from ultravioelt to the microwave," Appl. Opt., vol. 23, pp. 1206-1225, 1984.

[35] Kratz, D. P., "The correlated *k*-distribution technique as applied to the AVHRR channels," J. Quant. Spectrosc. Radiat. Transfer, vol. 53, 501-517, 1995.

[36] P. Minnis, L. Nguyen, D. R. Doelling, D. F. Young, W. F. Miller, and D. P. Kratz, "Rapid calibration of operational and research meteorological satellite imagers, Part II: Comparison of infrared channels," J. Atmos. Oceanic Technol., vol. 19, pp. 1250-1266, 2002.

[37] Q. Han, W. B. Rossow, and A. A. Lacis, "Near-global survey if effective droplet radii in liquid water clouds using ISCCP data," J. Climate, vol. 7, pp. 465-497, 1994.

[38] P. Minnis, P. W. Heck, S. Mayor, and D. F. Young, "A near-global analysis of cloud microphysical properties," *IRS '96: Current Problems in Atmospheric Radiation*, Ed. W. L. Smith and K. Stamnes, Deepak Publ. Hampton, VA, pp. 445-448, 1997.

[39] D. F. Young, P. Minnis, W. L. Smith, Jr., and D. P. Garber, "A four-channel method for deriving cloud radiative properties from meteorological satellite data," *IRS '96: Current Problems in Atmospheric Radiation*, Ed. W. L. Smith and K. Stamnes, Deepak Publ. Hampton, VA, pp. 612-615, 1997.

[40] M. A. Wetzel and L. L. Stowe, "Satellite-observed patterns in stratus microphysics, aerosol optical thickness, and shortwave radiative forcing," *J. Geophys. Res.*, vol. 104, pp. 31287–31299, 1999.

[41] K. Kawamoto, Nakajima, T., and T. Y. Nakajima, "A Global Determination of Cloud Microphysics with AVHRR Remote Sensing," *J. Climate*, vol. 14, pp. 2054–2068, 2001.

[42] Minnis, P., W. L. Smith, Jr., D. P. Garber, J. K. Ayers, and D. R. Doelling, 1995: Cloud properties derived from GOES-7 for the Spring 1994 ARM Intensive Observing Period using Version 1.0.0 of the ARM satellite data analysis program. *NASA RP 1366*, 59 pp.

[43] Berendes, T. A., K. S. Kuo, A. M. Logar, E. M. Corwin, R. M. Welch, B. A. Baum, A. Pretre, R. C.Weger, "A Comparison of paired histogram, maximum likelihood, class elimination, and neural network approaches for daylight global cloud classification using AVHRRimagery," *J. Geophys. Res.*, vol. 104, pp. 6199-6213, 1999.

[44] P. Minnis, J. Huang, B. Lin, Y. Yi, R. F. Arduini, T.-F. Fan, J. K. Ayers, and G. G. Mace, "Ice cloud properties in ice-over-water cloud systems using TRMM VIRS and TMI data," *J. Geophys. Res.*, vol. 112, D06206, doi:10.1029/2006JD007626, 2007.

[45] A. Mahesh, V. P. Walden, and S. G. Warren, "Radiosonde temperature measurements in strong inversions: Correction for thermal lag based on an experiment at the South Pole," *J. Atmos. Oceanic Technol.*, vol. 14, pp. 45-53, 1997.

[46] P. Minnis, P. W. Heck, D. F. Young, C. W. Fairall, and J. B. Snider, "Stratocumulus cloud properties derived from simultaneous satellite and island-based instrumentation during FIRE," *J. Appl. Meteorol.*, vol 31, pp. 317-339, 1992.

[47] R. D. Garreaud, J. Rutllant, J. Quintana, J. Carrasco, and P. Minnis, "CIMAR-5: A snapshot of the lower troposphere over the subtropical southeast Pacific," *Bull. Amer. Meteor. Soc.*, vol. 92, pp. 2193-2208, 2001.

[48] X. Dong, P. Minnis, B. Xi, S. Sun-Mack, and Y. Chen, "Comparison of CERES-MODIS stratus cloud properties with ground-based measurements at the DOE ARM Southern Great Plains site," *J. Geophys. Res.*, vol. 113, D03204, doi:10.1029/2007JD008438, 2008.

[49] P. Minnis and E. F. Harrison, "Diurnal variability of regional cloud and clear-sky radiative parameters derived from GOES data, Part II: November 1978 cloud distributions," *J. Clim. Appl. Meteorol.*, vol. 23, pp. 1012-1031, 1984.

[50] P. Minnis, D. F. Young, K. Sassen, J. M. Alvarez, and C. J. Grund, "The 27-28 October 1986 FIRE IFO Case Study: Cirrus parameter relationships derived from satellite and lidar data," *Mon. Wea. Rev.*, vol. 118, pp. 2402 – 2425, 1990.

[51] P. Minnis, P. W. Heck, and E. F. Harrison, "The 27-28 October 1986 FIRE IFO Case Study: Cloud parameter fields derived from satellite data," *Mon. Wea. Rev.*, vol. 118, 2426- 2446, 1990.

[52] V. Chakrapani, D. R. Doelling, A. D. Rapp, and P. Minnis, "Cloud thickness estimation from GOES-8 satellite data over the ARM SGP site," Proc. 12th ARM Science Team Meeting, April 8-12, St. Petersburg, FL, 14 pp, 2002. Available at http://www.arm.gov/publications/proceedings/conf12/extended_abs/chakrapani-v.pdf.

[53] W. L. Smith, Jr., P. Minnis, J. M. Alvarez, T. Uttal, J. M. Intrieri, T. P. Ackerman, and E. E. Clothiaux, "Development of methods for inferring cloud thickness and cloud-base height from satellite radiance data," *The FIRE Cirrus Science Results 1993*, David S. McDougal, ed., NASA CP-3238, pp. 32–35, 1993.

[54] Caldwell, T. E., et al., "Clouds and the Earth's Radiant Energy System (CERES) Data Management System Data Products Catalog, Release 4 Version 16," 240 pp., February 2008. Available at http://eosweb.larc.nasa.gov/PRODOCS/ceres/DPC/.

[55] Minnis, P., L. Nguyen, R. Palikonda, P. W. Heck, D. A. Spangenberg, D. R. Doelling, J. K. Ayers, W. L. Smith, Jr., M. M. Khaiyer, Q. Z. Trepte, L. A. Avey, F.-L. Chang, C. R. Yost, T. L. Chee, and S. Sun-Mack, 2008: Near-real time cloud retrievals from operational and research meteorological satellites. *Proc. SPIE Europe Remote Sens. 2008*, Cardiff, Wales, UK, 15-18 September, **7107-2**, 8 pp.

[56] Minnis, P., L. Nguyen, R. Palikonda, J. K. Ayers, R. F. Arduini, F.-L. Chang, T. L. Chee, D. R. Doelling, P. W. Heck, M. M. Khaiyer, M. L. Nordeen, W. L. Smith, Jr., D. A. Spangenberg, C. R. Yost, P. Yang, and Y. Xie, 2009: Cloud properties determined from GOES and MODIS data during TC4. Submitted to *J. Geophys. Res.*

Table 1. IGBP surface types (general type used for model selections).

1. evergreen needleleaf (conifer)	11. permanent wetlands (1/2 grass + 1/2 water)
2. evergreen broadleaf (conifer)	12. croplands = grass
3. deciduous needleleaf (deciduous)	13. urban
4. deciduous broadleaf (deciduous)	14. mosaic (1/2 grass + 1/2 mixed forest)
5. mixed forests (1/2 conifer + 1/2 deciduous)	15. snow/ice
6. closed shrublands (mosaic)	16. barren/sparsely vegetated (desert)
7. open shrubland (mosaic)	17. water
8. woody savannas (grass)	18. tundra (1/2 grass + 1/2 water)
9. savannas (grass)	19. coastline (10% to 90% water)
10. grasslands (grass)	

Table 2. Central wavelengths (μm) for VIRS and MODIS channels

Channel	VIRS	MODIS
1	0.625	0.646
2	1.609	1.629
2 (Aqua)	--	2.114
3	3.787	3.792
4	10.75	11.03
5	11.95	12.02

Table 3. Average dimensions of hexagonal ice columns used in retrievals.

D_e	Volume (μm^3)	Area (μm^2)
5.83	0.12208E+03	0.37767E+02
18.15	0.11549E+04	0.10387E+03
23.86	0.68868E+04	0.47257E+03
30.36	0.11001E+05	0.58102E+03
41.20	0.27780E+05	0.10328E+04
45.30	0.22795E+05	0.73791E+03
67.60	0.53529E+05	0.12299E+04
75.2	0.16837E+06	0.31445E+04
104.9	0.33546E+06	0.43636E+04
123.1	0.57019E+06	0.61101E+04
134.9	0.17196E+07	0.16540E+05

Table A1. Relative differences in TOA reflectance between parameterization and AD calculations.

a_{sd} (%)	new parameterization	old parameterization
4-10	-0.01 $\pm$ 0.53 %	-0.08 $\pm$ 5.1 %
10 -50	-0.01 $\pm$ 0.67 %	-0.14 $\pm$ 7.0 %
50-90	0.03 $\pm$ 1.04 %	-4.3 $\pm$ 12.4 %

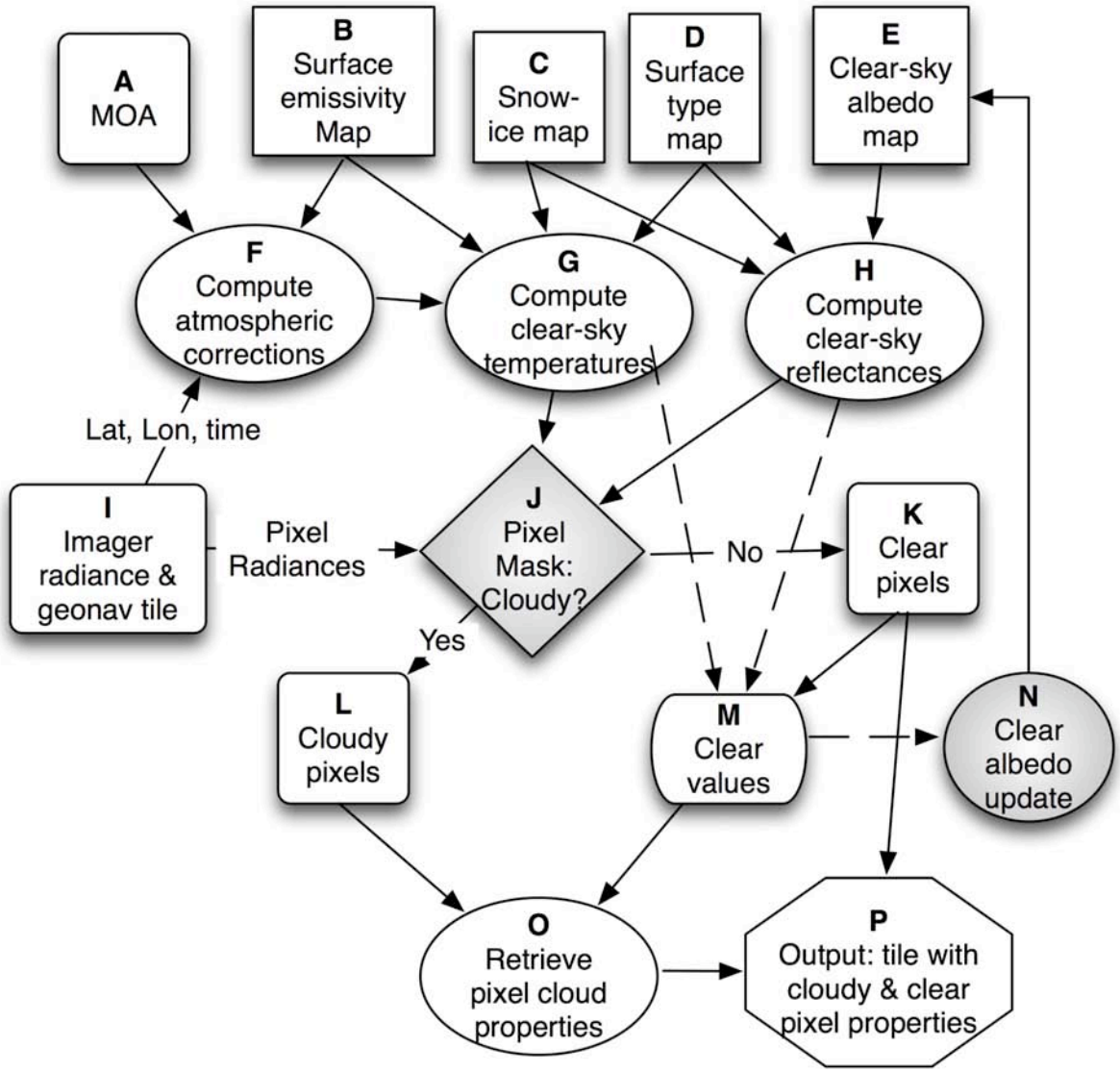

Fig. 1. CERES cloud processing scheme. Algorithms corresponding to shaded boxes are discussed in [5].

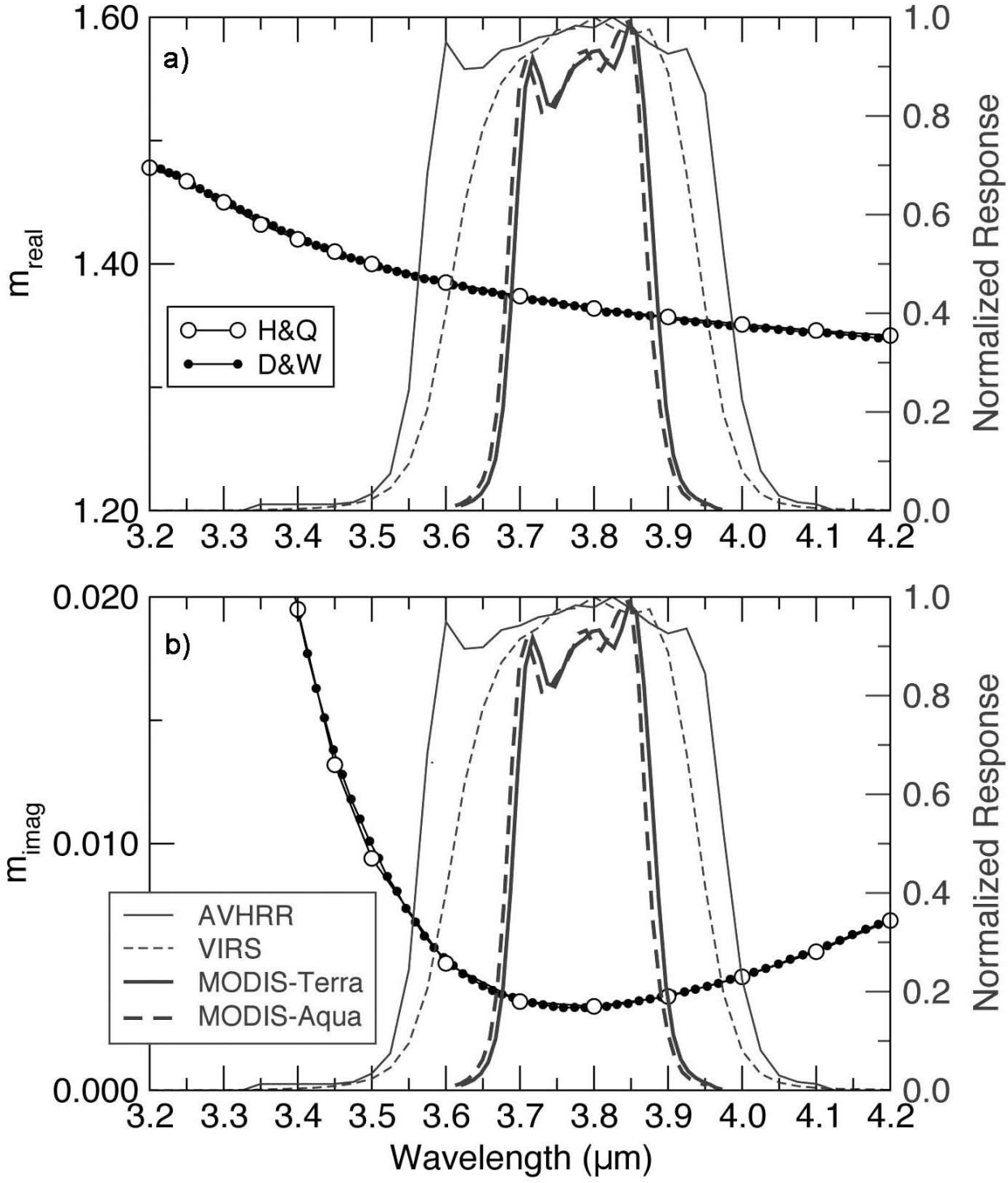

Fig. 2. Spectral filter functions for the SIR bands on several imagers. (a) Real and (b) imaginary indices of refraction *m* for liquid water also plotted for two sources, H&Q [32] and D&W [34].

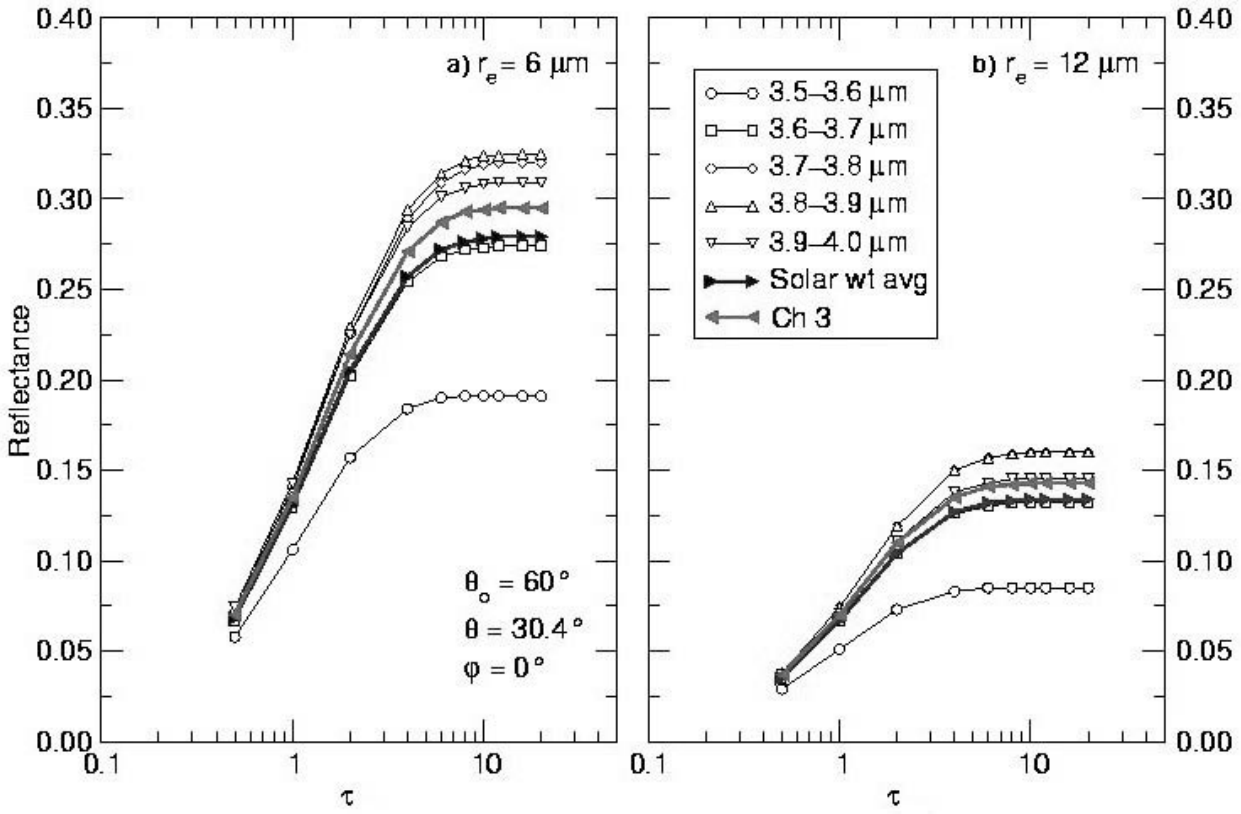

Fig. 3. Reflectances computed for the MODIS 3.78-µm channel and sub-bands for a liquid water cloud. Ch 3 denotes calculations for effective wavelength.

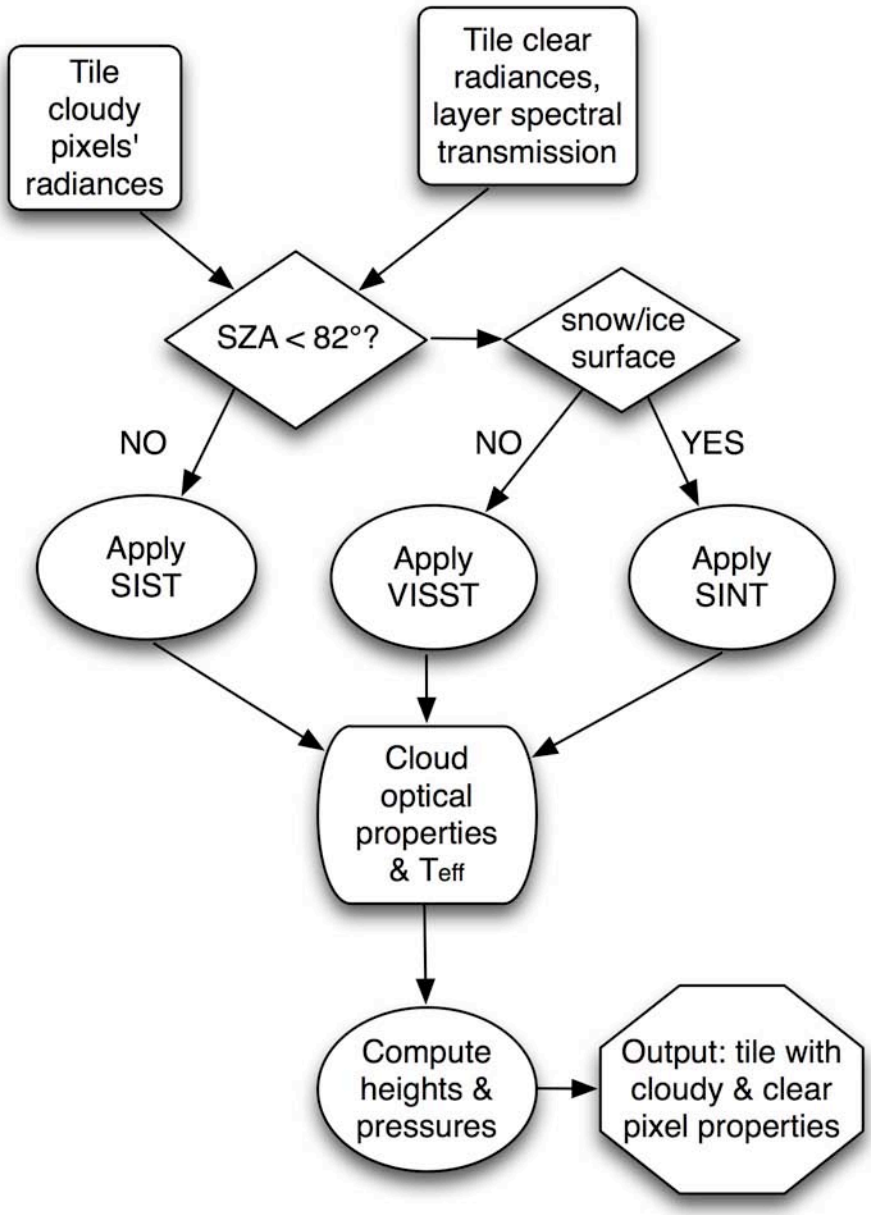

Fig. 4. Overview of CERES Cloud Property Retrieval System (CPRS) in Box O from Fig. 1.

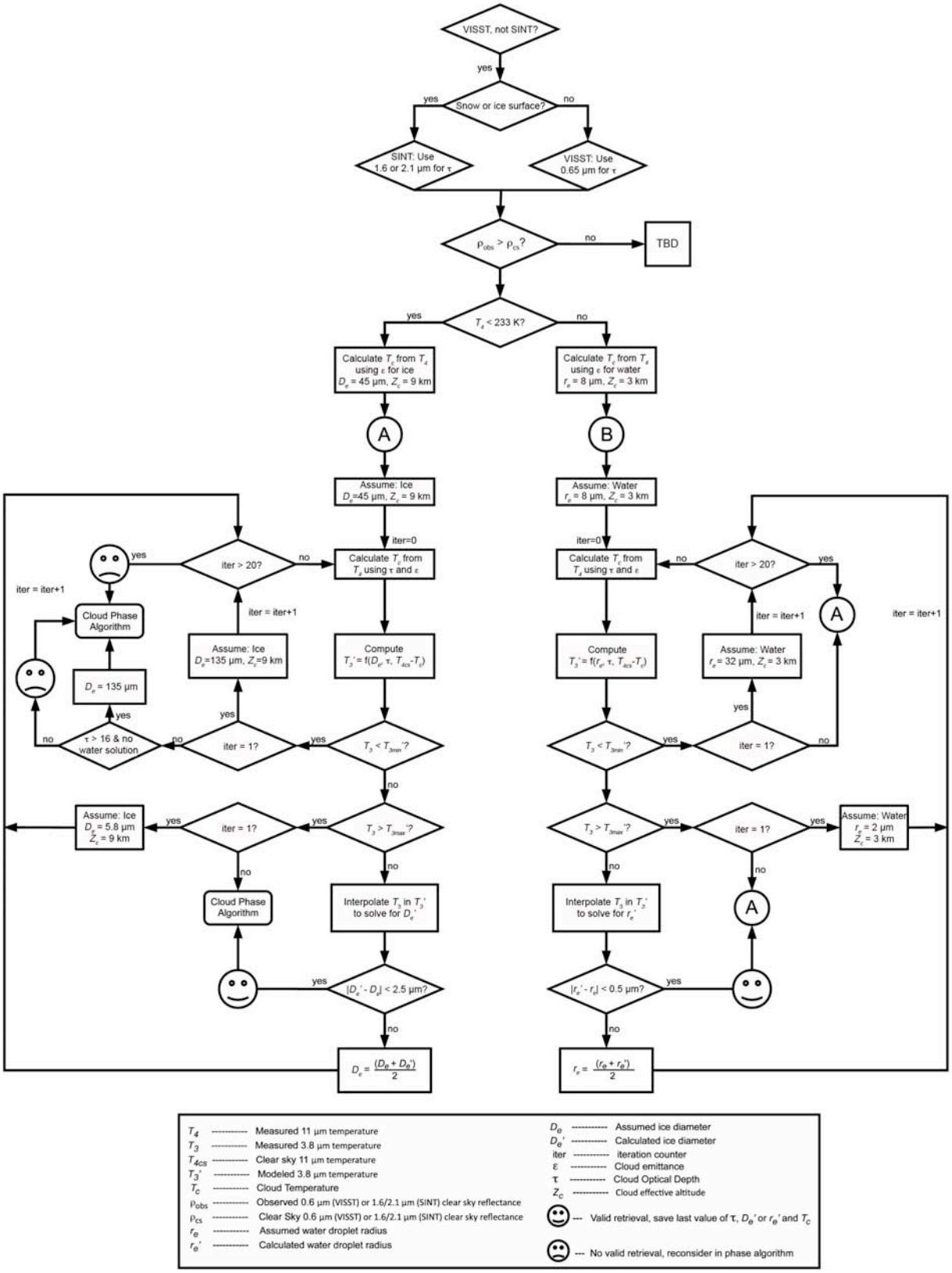

Fig. 5. Flowchart of VISST analysis process.

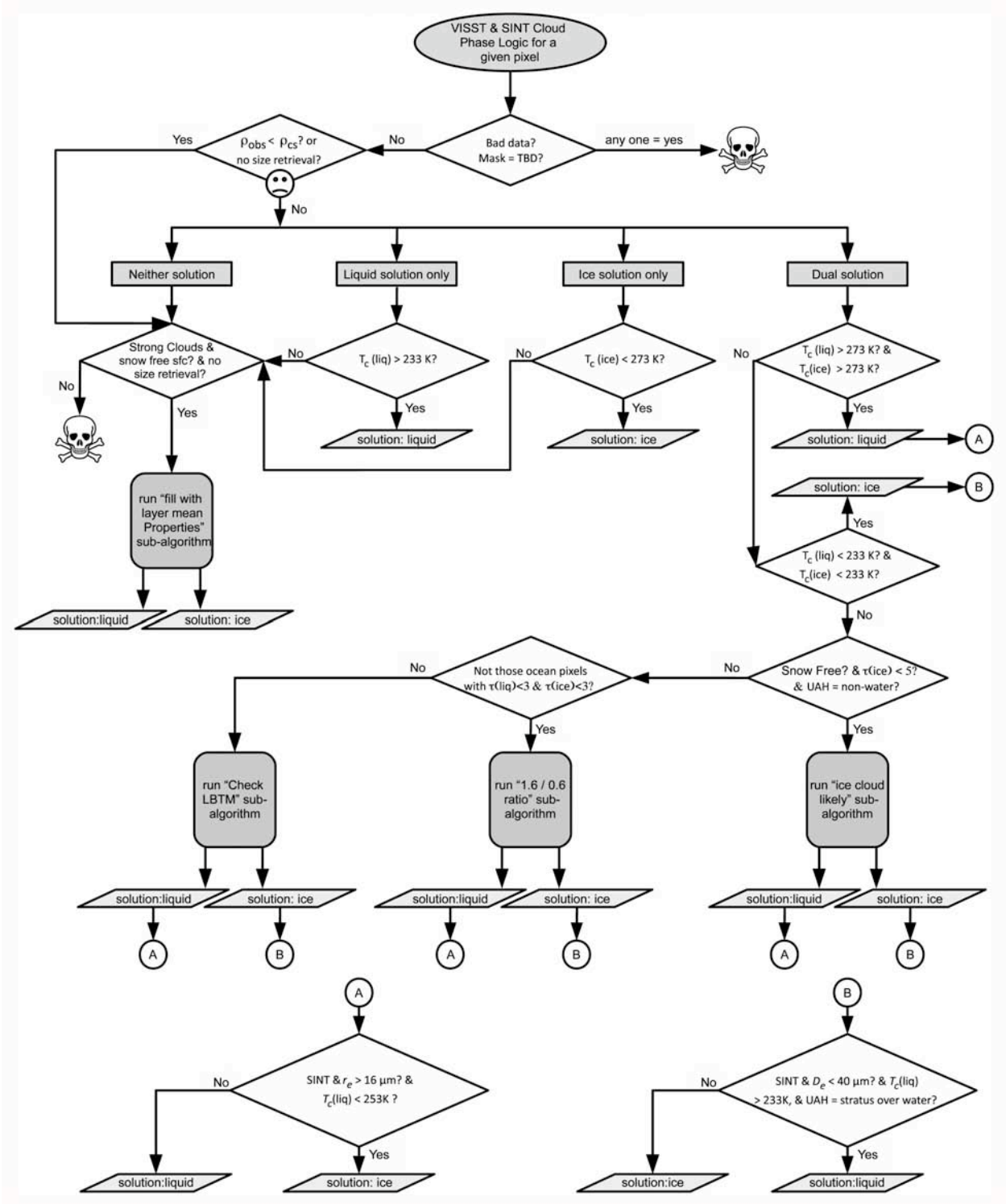

Fig. 6. Phase selection algorithm for Aqua Ed2 daytime retrieval algorithm.

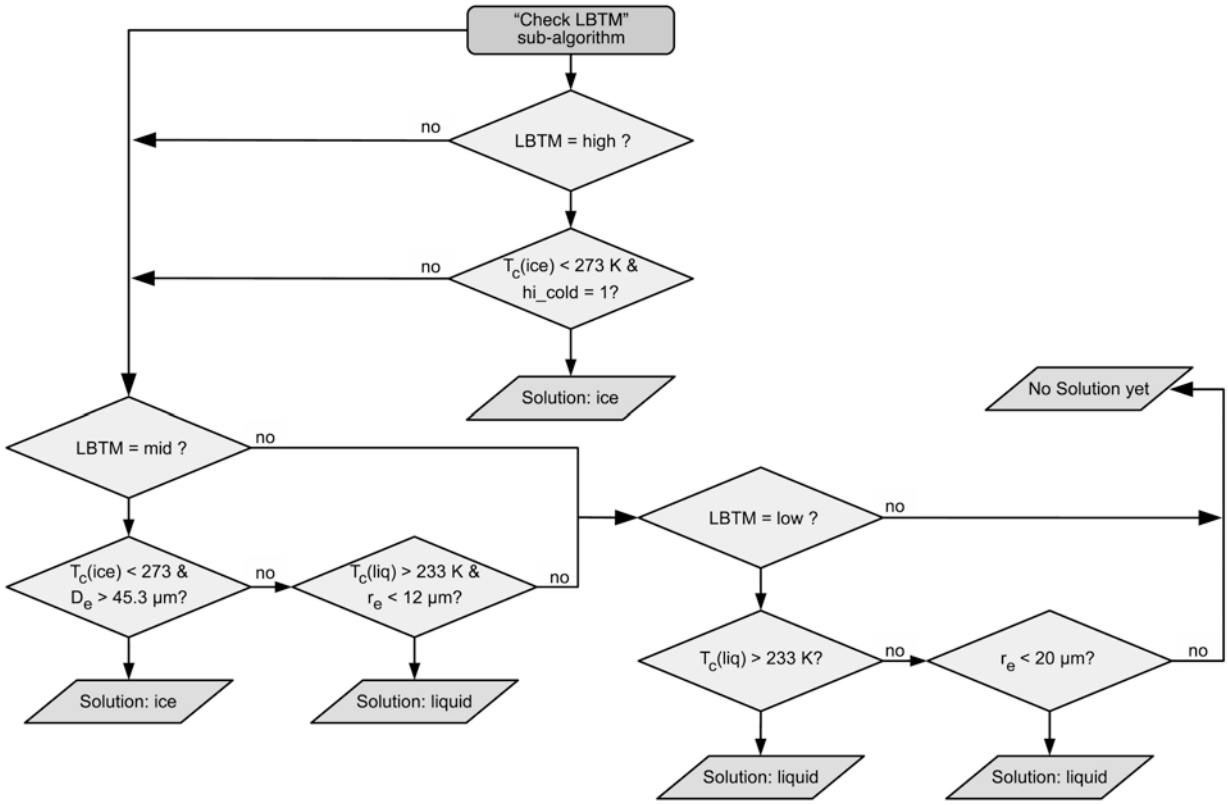

Fig. 7. Further phase determination logic for Aqua Ed2 algorithm called from within the main decision tree in Fig. 6: (b) ice cloud likely check.

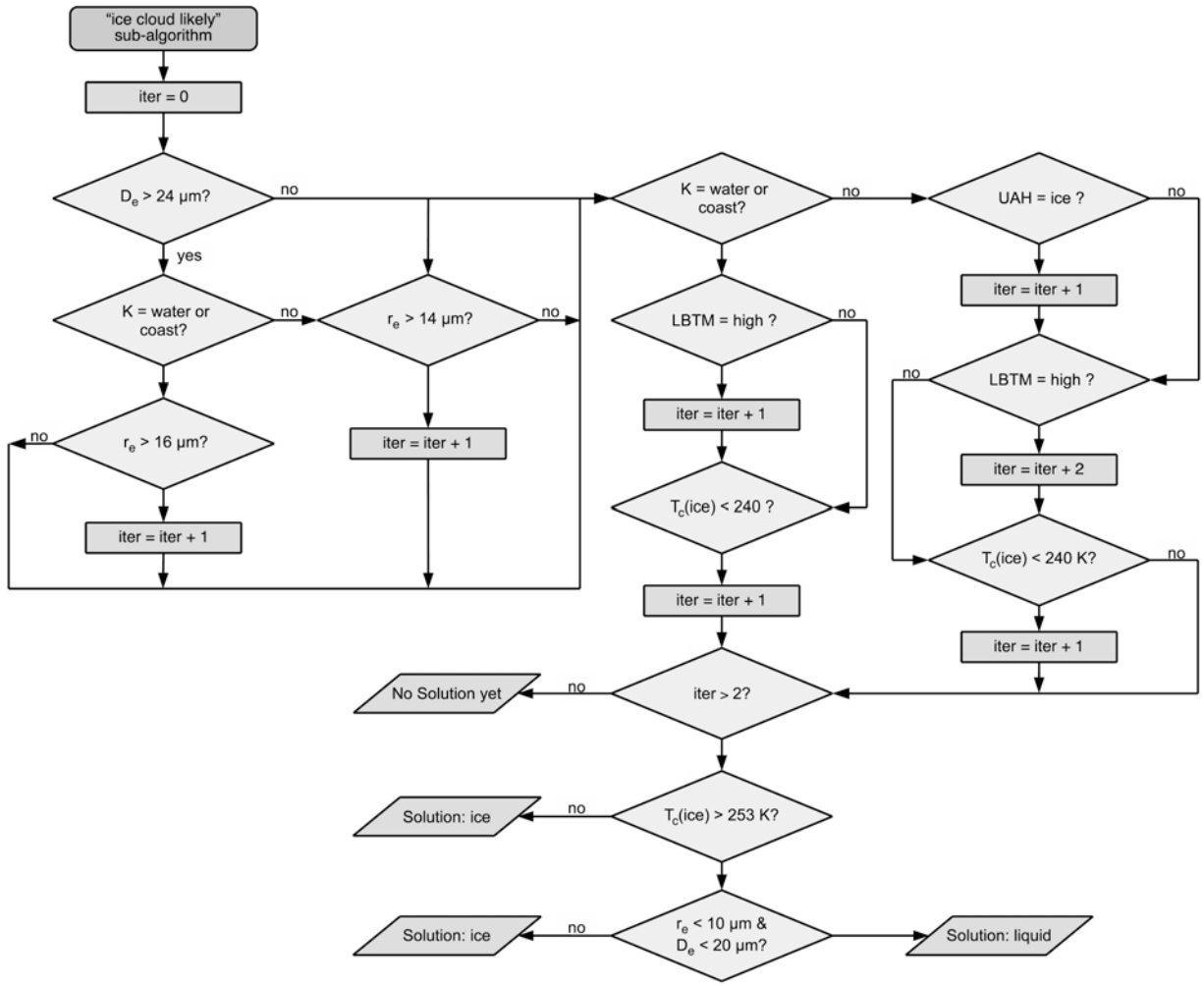

Fig. 7. Further phase determination logic for Aqua Ed2 algorithm called from within the main decision tree in Fig. 6: (b) ice cloud likely check.

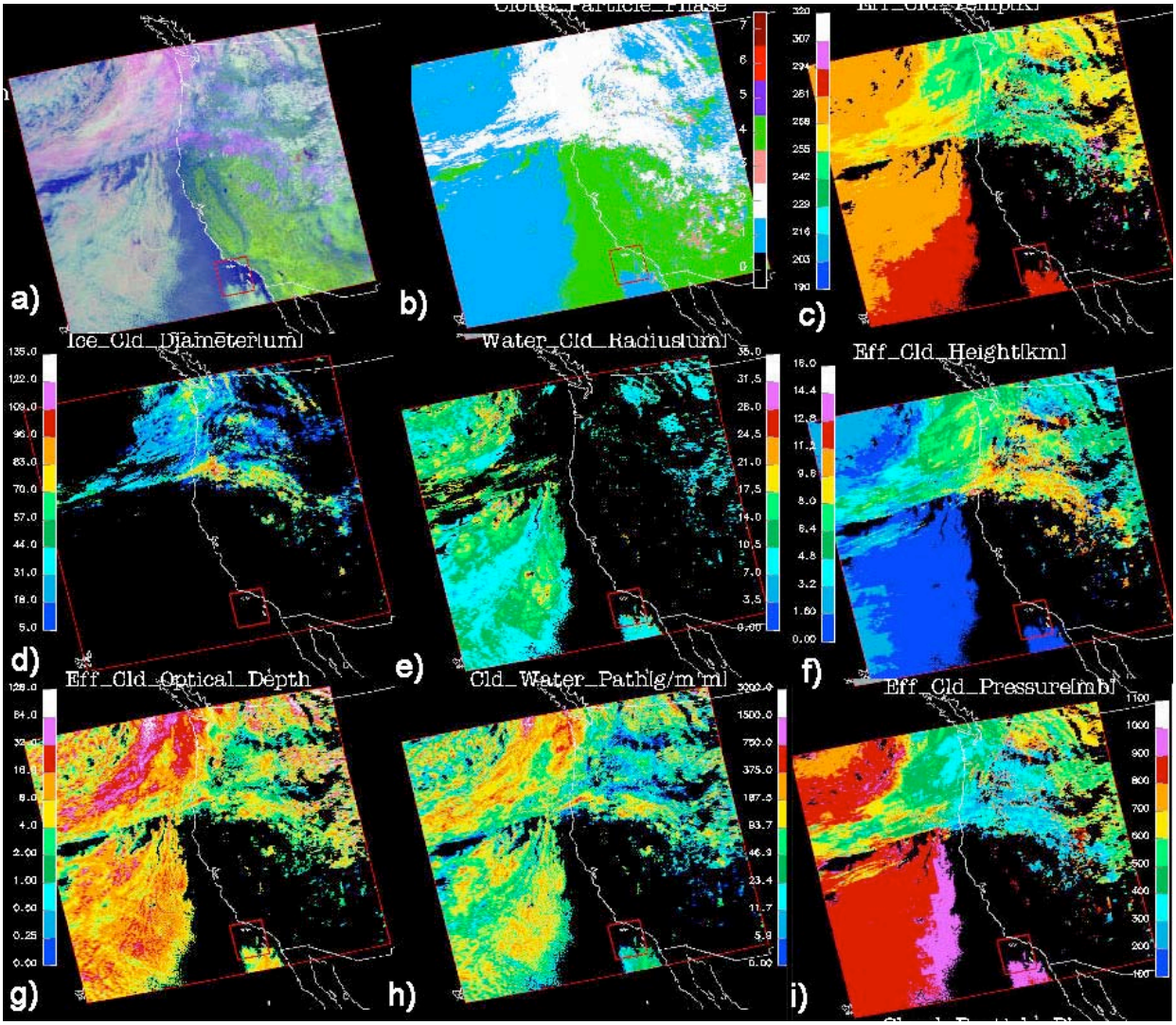

Fig. 8. Cloud properties derived by applying the VISST to daytime Terra MODIS data taken over western North America and the eastern Pacific, 21 UTC, 12 June 2004. (a) RGB image, (b) Phase, (c) T_c (K), (d) D_e (μm), (e) r_e (μm), (f) Z_c, (g) t, (h) ice/liquid water path (g m^{-2}), (i) p_c (hPa).

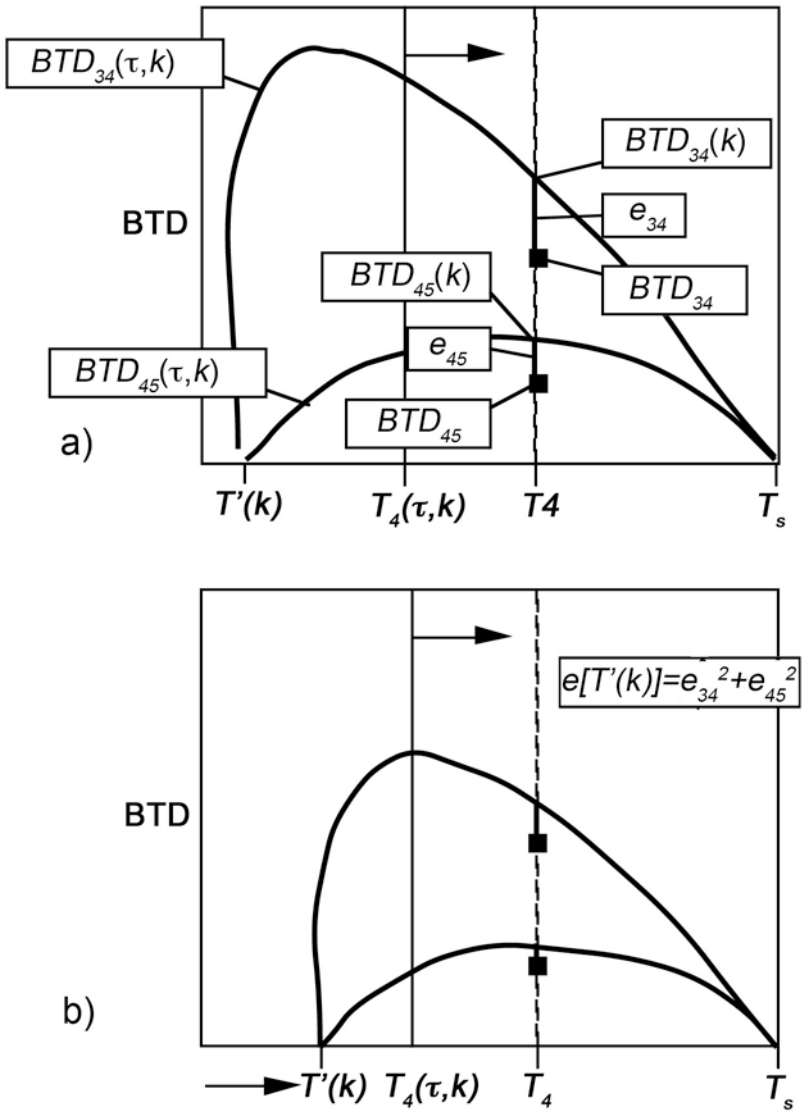

Fig. 9. Schematic illustration of SIST iteration process for nocturnal retrievals. (a) Step 1, compute errors for model *k* using first guess temperature. (b) Step 2, compute errors for second temperature estimate.

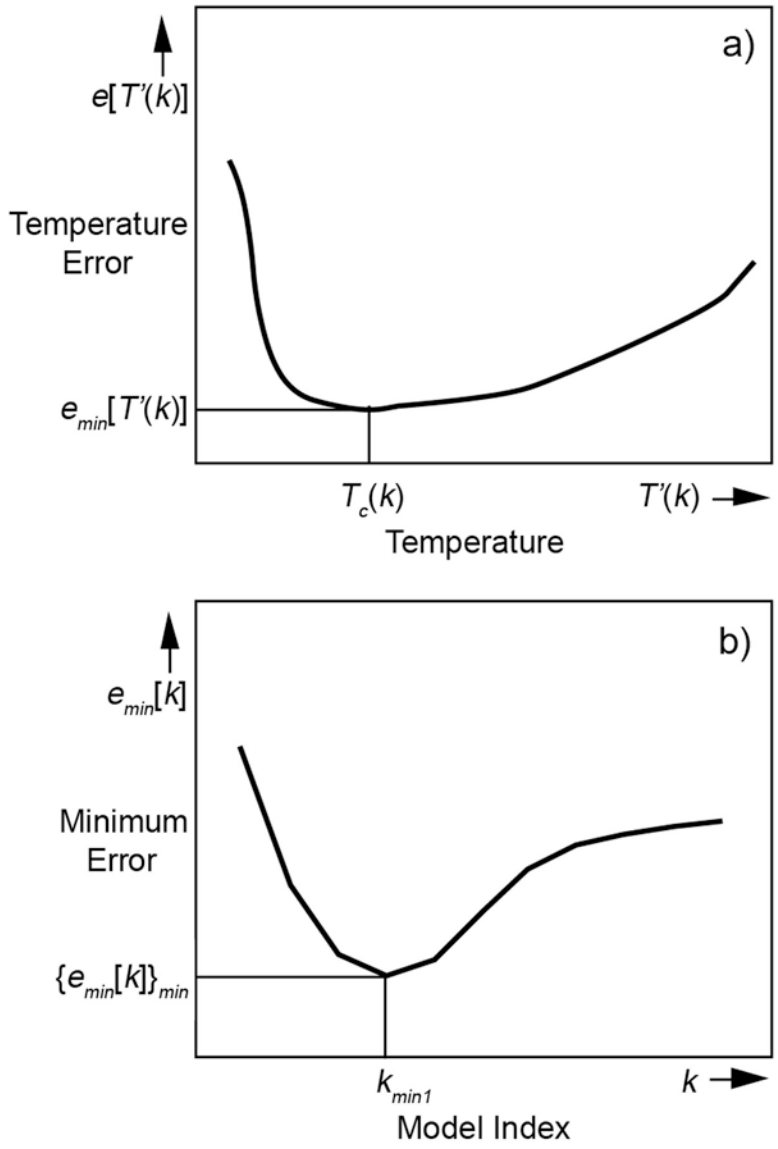

Fig. 10. Schematic diagram of minimum error estimation to determine most likely particle size models. (a) Determining minimum error for a given particle size model. (b) Determining model having minimum error.

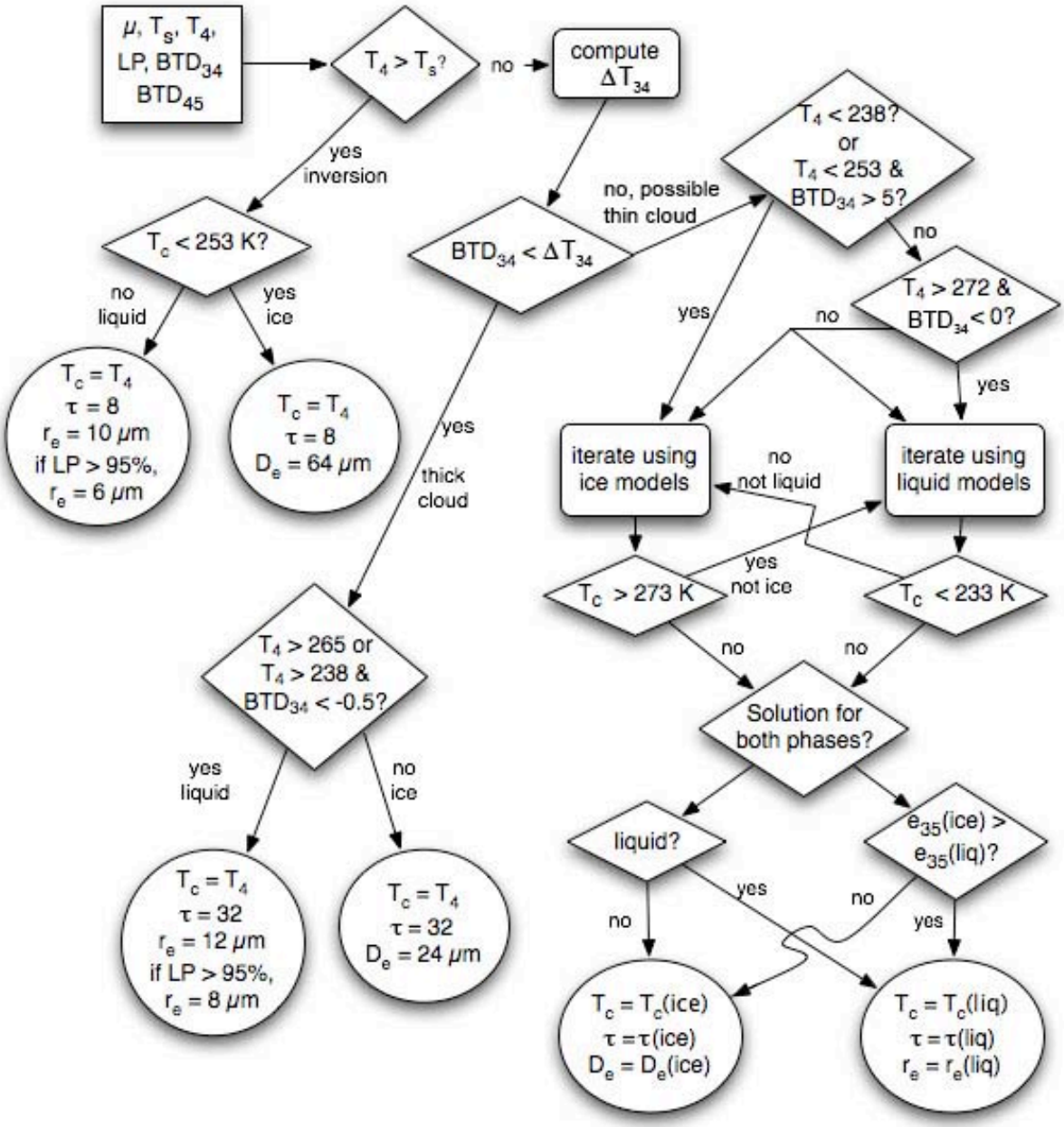

Fig. 11. Flow diagram of SIST used for cloud property retrievals during nighttime and twilight conditions.

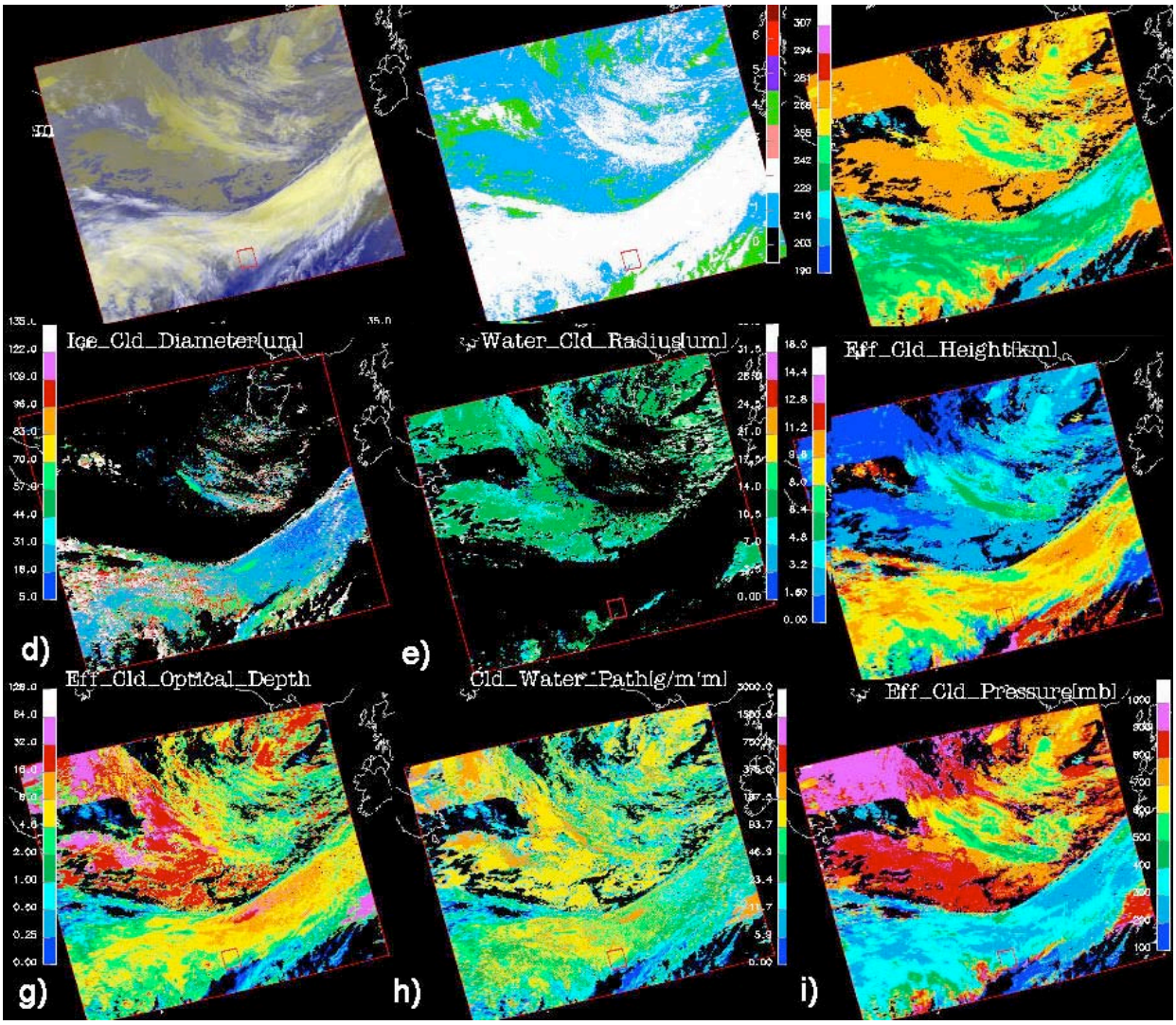

Fig. 12. Cloud properties derived by applying the SIST to nighttime Aqua MODIS data taken over the North Atlantic, 23 UTC, 22 May 2004. (a) RGB image, (b) Phase, (c) T_c (K), (d) D_e (μm), (e) r_e (μm), (f) Z_c, (g) t, (h) ice/liquid water path (g m^{-2}), (i) p_c (hPa).

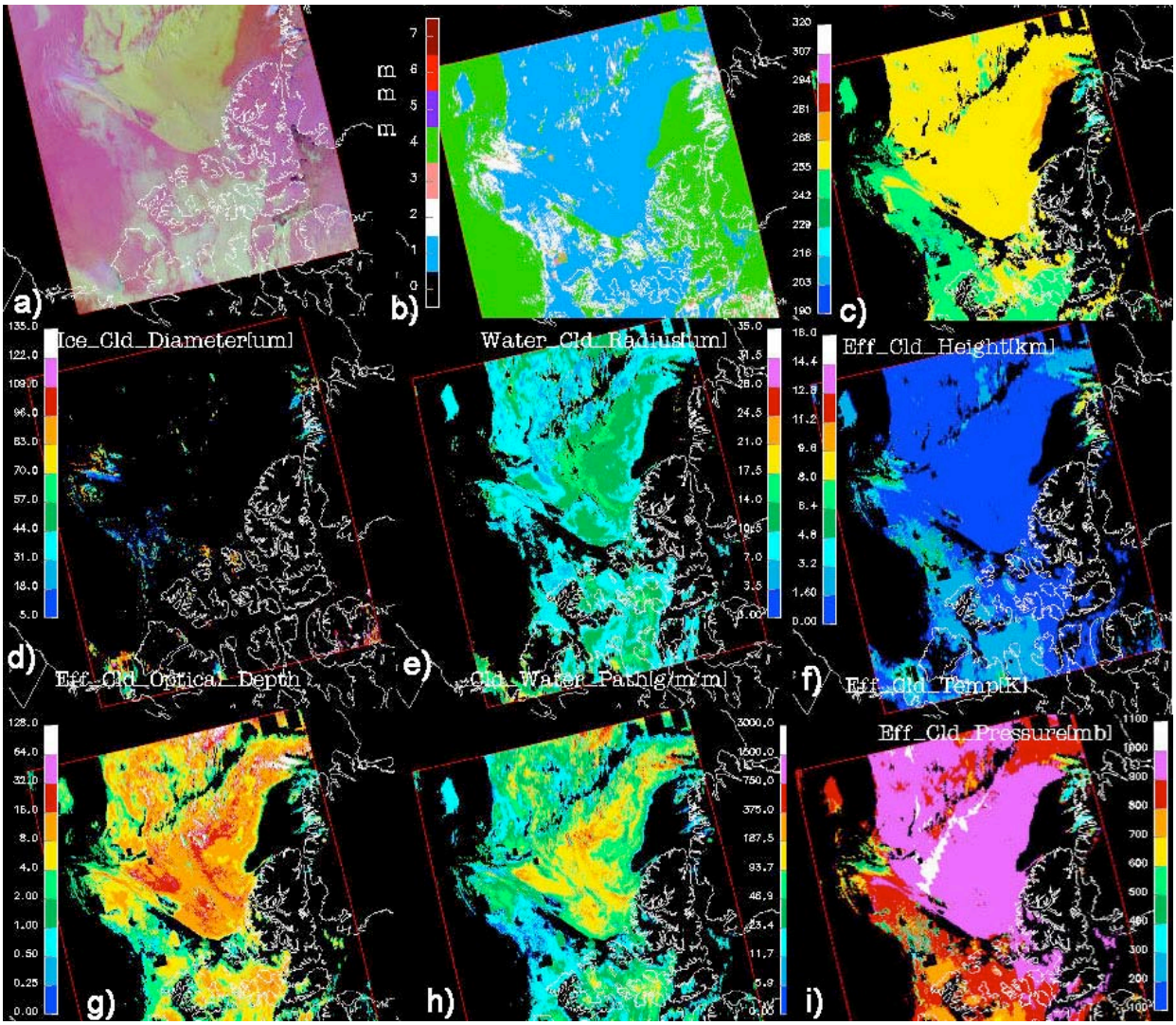

Fig. 13. Cloud properties derived during daytime by applying the SINT to Terra MODIS data taken over north central Canada and the adjacent Arctic Ocean, 23 UTC, 3 May 2005. (a) RGB image, (b) Phase, (c) T_c (K), (d) D_e (μm), (e) r_e (μm), (f) Z_c, (g) t, (h) ice/liquid water path (g m^{-2}), (i) p_c (hPa).

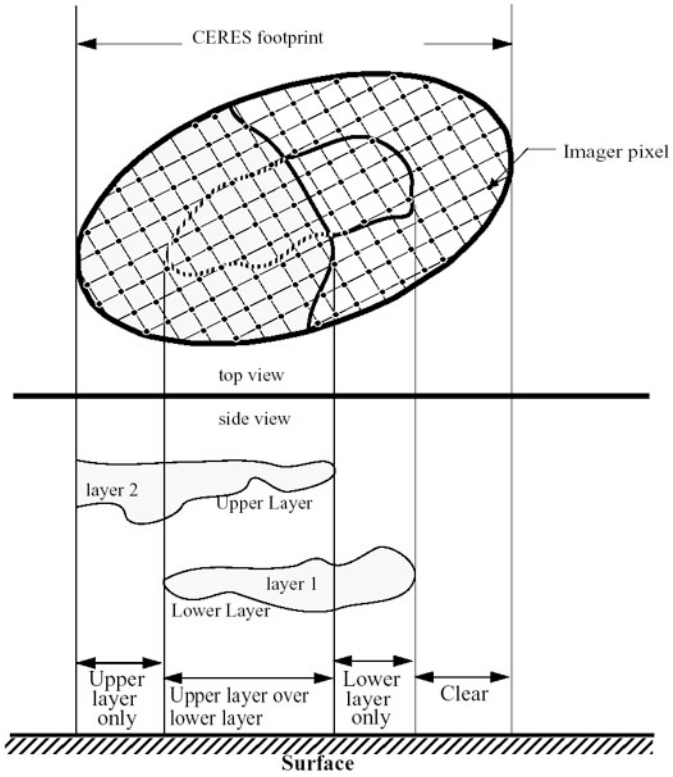

Fig. 14. Illustration of CERES SSF constructed for a scene containing two cloud layers and some clear imager pixels.